TRIBHUVAN UNIVERSITY

INSTITUTE OF ENGINEERING

PULCHOWK CAMPUS

THESIS NO : M-82-MSMDE-2021-2023

**Aeroelastic Study of Detonation Waves Formed over the Ramp Structure of
Oblique Detonation Wave Engine**

by

Sandip Gewali

A THESIS SUBMITTED TO THE DEPARTMENT OF MECHANICAL AND
AEROSPACE ENGINEERING IN PARTIAL FULFILLMENT OF THE
REQUIREMENTS FOR THE DEGREE OF MASTERS OF SCIENCE IN
MECHANICAL SYSTEMS DESIGN AND ENGINEERING

DEPARTMENT OF MECHANICAL AND AEROSPACE ENGINEERING

LALITPUR, NEPAL

NOVEMBER, 2023

COPYRIGHT

TRIBHUVAN UNIVERSITY

INSTITUTE OF ENGINEERING

PULCHOWK CAMPUS

DEPARTMENT OF MECHANICAL AND AEROSPACE ENGINEERING
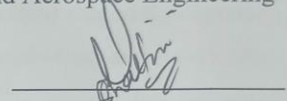
The undersigned certify that they have read, and recommended to the Institute of Engineering for acceptance, a thesis titled '**Aeroelastic Study of Detonation Waves Formed over the Ramp Structure of Oblique Detonation Wave Engine**' submitted by **Sandip Gewali (078/MSMDE/014)** in partial fulfillment of the requirements for the degree of Masters in Mechanical Systems Design and Engineering.

Assoc. Prof. Dr. Nawraj Bhattrai

Supervisor

Department of Mechanical and Aerospace Engineering

Asst Prof. Sudip Bhattrai, Ph. D.

Supervisor

Department of Mechanical and Aerospace Engineering

Dr. Abhas Maskey,

External Examiner,

Antarikchya Pratisthan Nepal (APN)

Committee Chairperson, Asst Prof. Sudip Bhattrai

Head of the Department

Department of Mechanical and Aerospace Engineering

Date: 2023/11/26

iii

ABSTRACT

Oblique Detonation Wave Engines have gained a lot of research interest due to their higher total pressure recoveries and shorter combustor lengths. However, for a ramp-induced type detonation, extreme temperature and pressure loadings cause ramps to deflect, decr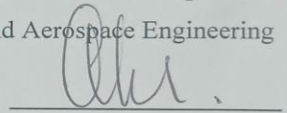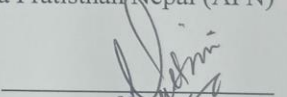ease the effective ramp angle and hence alter the detonation wave properties. This study aims to study the aeroelastic response of such compliant ramp structures and assess their vibrational properties. Moreover, considering two compliant ramps of horizontal length 100 mm and 150 mm, which when rigid, admit near-to-zero mass spillage from the combustor to the nozzle were studied by coupling an in-house OpenFOAM-based solver rhoCentralReactingFoam with an open-source FEM solver Calculix coupled with coupling library - preCICE. Their responses indicated that their forced response is first-mode dominated and the induction zone of oblique detonations move along the ramp with first-mode dominant response. Viscous simulation of the reactive flow-field along with inclusion of temperature-dependent material properties of the ramp structure is suggested to conduct fluid-thermal-structural-interaction studies.

ACKNOWLEDGEMENT

TABLE OF CONTENTS

LIST OF FIGURES

LIST OF TABLES

LIST OF SYMBOLS

∇	Gradient
$\dfrac{\partial}{\partial t}$	Temporal derivative
δ_x, δ_y	Displacement in x and y-direction
#	Number
ω	Natural frequency of vibration
$\vec{\emptyset}$	Convective face flux
ρ	Density
$a_{n,i}$	NASA polynomial coefficients for species i
A	Interface area
$\overline{c_p}$	Mixture's mean specific heat at constant pressure (in mass units)
$c_{p,i}$	Constant pressure specific heat (in mass units) of specie i
$C_{p,i}$	Constant pressure specific heat (in molar units) of specie i
$c_{v,i}$	Constant volume specific heat (in mass units) of specie i
$C_{v,i}$	Constant volume specific heat (in molar units) of specie i
E	Modulus of Elasticity, Total Energy
g	Gram
$\vec{g}$	Volumetric (Gravitational) loading
h	Specific enthalpy, Thickness of cantilever beam
H	Enthalpy
I_z	Moment of Inertia about z-axis
k	Reaction rate constant
K	Kelvin
L	Length of cantilever beam
m	Meter

M, Ma	Mach number
(n_x, n_y, n_z)	Number of cells in x, y and z-direction
N	Newton
p	Pressure
R	Specific gas constant
s	Second
T	Temperature
u	Velocity
u_0	Combustion wave velocity
U_i	Internal energy of specie i
v	Specific volume
w	Width of cantilever beam
$\overline{W}$	Apparent (mean) molecular weight of mixture
W_i	Molecular weight of species i
x	Specific volume ratio of products and reactants
$\dot{x}_i$	Specie molar production rate
X_{CJ}	Property X corresponding to Chapman-Jouguet condition
X_i	Molar fraction of species i
X_{VN}	Property X corresponding to Von-Neumann spike
y	Pressure ratio of products and reactants
Y_i	Mass fraction of species i

LIST OF ABBREVIATIONS

CFD	Computational Fluid Dynamics
CHT	Conjugate Heat Transfer
CJ	Chapman-Jouguet
ER	Equivalence Ratio
FEM	Finite Element Method
FFT	Fast Fourier Transform
FSI	Fluid-Structure Interaction
GCI	Grid Convergence Index
Hz	Hertz
LES	Large Eddy Simulation
NASA	National Aeronautics and Space Administration
OD	Oblique Detonation
ODW	Oblique Detonation Wave
ODWE	Oblique Detonation Wave Engine
OpenFOAM	Open-source Field Operation and Manipulation
preCICE	Precise Code Interaction Coupling Environment
RANS	Reynolds Averaged Navier-Stokes
SSTO	Single Stage To Orbit
TVD	Total Variation Diminishing
UCF	University of Central Florida
UDL	Uniformly Distributed Load
URANS	Unsteady Reynolds Averaged Navier-Stokes

CHAPTER ONE: INTRODUCTION

1.1 Background

The exploration of feasible combustion waves under defined initial and boundary conditions involves solving conservation equations governing steady one-dimensional (1D) flow for reactants, which transform into products upon interaction with a combustion wave. This process necessitates the formulation and resolution of an equation of state for both reactants and products, accompanied by three fundamental conservation equations: continuity, momentum, and energy. These equations collectively constitute a system of four equations aiming to determine five unknown quantities—specifically, the initial state variables (pressure denoted as p_1, density as ρ_1, velocity as u_1, enthalpy as h_1) and the velocity of the combustion wave (u_0). To achieve closure within this set of equations, an additional equation is required, signifying the need for a comprehensive framework for solution attainment. The foundational groundwork for conservation equations concerning non-reacting gases was laid by Rankine in 1870 and subsequently expanded upon by Hugoniot between 1887 and 1889. In Figure 1.1, the reactants positioned at state 0 exhibit defined properties encompassing pressure (p_0), density (ρ_0), and enthalpy (h_0), transitioning into products characterized by distinct properties—pressure (p_1), density (ρ_1), and enthalpy (h_1). These eminent researchers established critical relationships between upstream and downstream states in terms of specific particle velocities, pressures, or wave speeds post the occurrence of a shock wave. The outcomes of the analysis of conservation equation solutions, as presented by (Lee, 2008), unveiled pivotal insights into the stability of shock waves and the inherent limitations surrounding the formation of rarefaction shocks within the majority of commonplace fluids. This analytical examination provided profound revelations regarding the nature of shock wave stability, while also shedding light on the unlikelihood of rarefaction shocks in typical fluid scenarios. The process of understanding feasible combustion waves necessitates the resolution of conservation equations governing steady 1D flow for reactants evolving into products in the presence of a combustion wave. This requires an equation of state for both reactants and products, coupled with three essential conservation equations—continuity, momentum, and energy. Solving these equations results in a system of four equations aiming to determine five unknown quantities: pressure (p_1),

density (ρ_1), velocity (u_1), enthalpy (h_1), and the combustion wave velocity (u_0). To complement this system, an additional equation is indispensable, emphasizing the need for a comprehensive solution framework. Rankine and Hugoniot laid the groundwork for conservation equations governing non-reacting gases in the late 19th century. Figure 1.1 delineates the properties of reactants (state 0) comprising pressure (p_0), density (ρ_0), and enthalpy (h_0), transitioning into products characterized by distinct properties—pressure (p_1), density (ρ_1), and enthalpy (h_1). Their groundbreaking work established vital relationships between upstream and downstream states concerning specific particle velocities, pressures, or wave speeds subsequent to the occurrence of a shock wave. Lee provided profound insights into the stability of shock waves and the dearth of rarefaction shocks within typical fluid mediums. This study unveiled critical understandings regarding shock wave stability and the infrequency of rarefaction shocks in the prevailing scenarios involving common fluids (Lee, 2008).
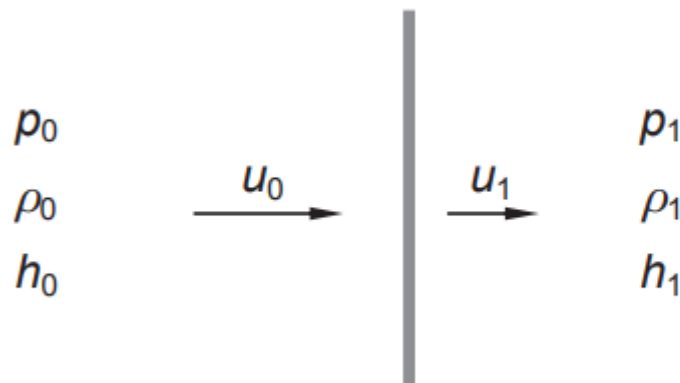
Figure 1.1: One-dimensional steady flow across a combustion wave in wave-fixed coordinate system (Lee, 2008)

Analyzing the conservation laws governing reacting mixtures originated independently through the investigations of Chapman in 1889, Jouguet in 1904, and Crussard in 1907. It's noteworthy that these researchers, despite their seminal contributions, conducted their studies without awareness of similar endeavors carried out by Mikelson in Russia in 1890. Subsequently, a more comprehensive examination of the mathematical and physical properties of solutions to these conservation laws was pursued by a cohort of researchers including von Neumann in 1942, Zeldovich spanning 1940 to 1950, Doring in 1943, Kistiakowsky and Wilson in 1941, and Becker between 1917 and 1922. Their

collective aim centered on fortifying the theoretical underpinning of the Chapman–Jouguet criterion, delving into the intricacies surrounding the conversion process from reactants to products—charted along the Rayleigh line from the initial state (x = y = 1) to a final state (x, y) that intersects the Hugoniot curve. Solutions derived from these conservation laws necessitate the concurrent satisfaction of both the Hugoniot curve and the Rayleigh line. As such, distinct solutions emerge: weak and strong deflagrations on the lower branch and a pair of solutions on the upper branch referred to as strong and weak detonations, as visually represented in Figure 1.2. These solutions manifest as a couple of potential outcomes in the (x, y) domain corresponding to a given combustion wave propagation velocity—the slope of the Rayleigh line. Notably, the Hugoniot curve exhibits its minimum velocity along the detonation branch and its maximum velocity on the deflagration branch, where these two solutions converge at the juncture where the Rayleigh line tangentially intersects the curve. These tangential points denote the CJ solutions—critical junctures pivotal in defining the wave behavior. In scenarios where the Rayleigh line fails to intersect the Hugoniot curve, no solution exists within that framework (Lee, 2008).
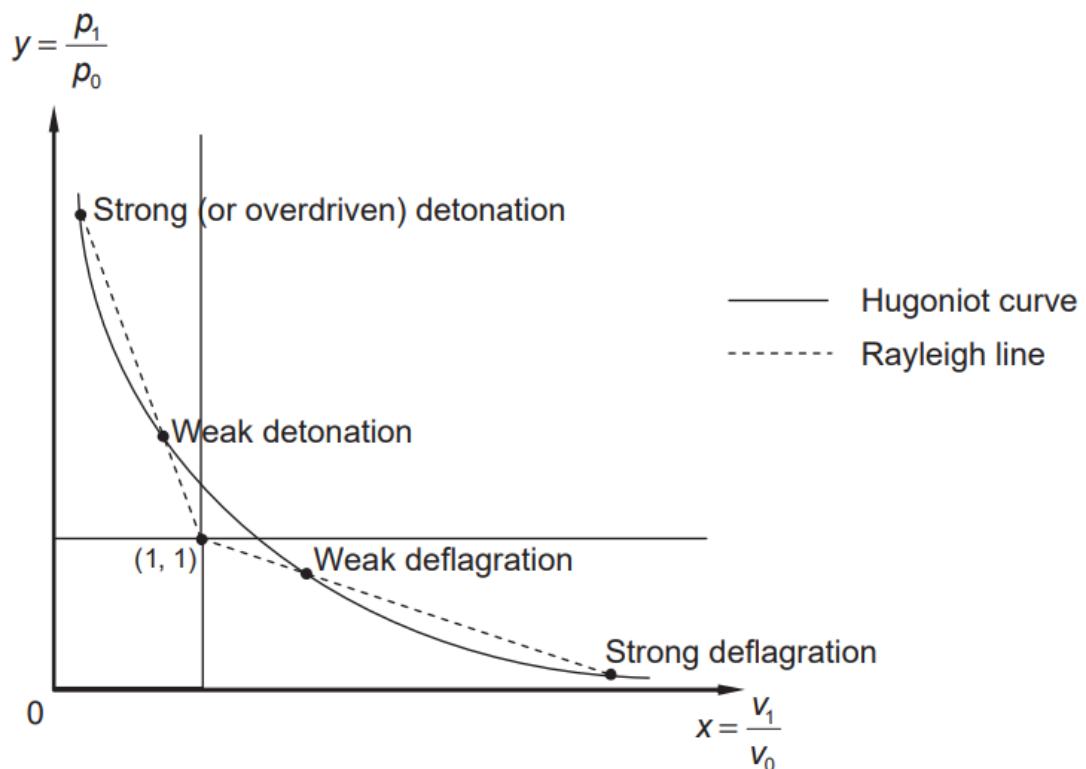
Figure 1.2: The Rayleigh line and the Hugoniot curve (Lee, 2008)

3

Hence, in the p-v plane, domains of detonation and deflagration combustion waves look as shown in Figure 1.3. Considering (p, v) = (1, 1) as the origin, solutions in the first and third quadrant are not possible since the slope of the Rayleigh line becomes negative in such cases. Thus, detonations and deflagrations occur for conditions pertaining to the second and fourth quadrant respectively.

$$y = \frac{p_1}{p_0}$$

Detonation
$y > 1$ and $x < 1$

1

Deflagration
$y < 1$ and $x > 1$

$$x = \frac{v_1}{v_0}$$

0   1
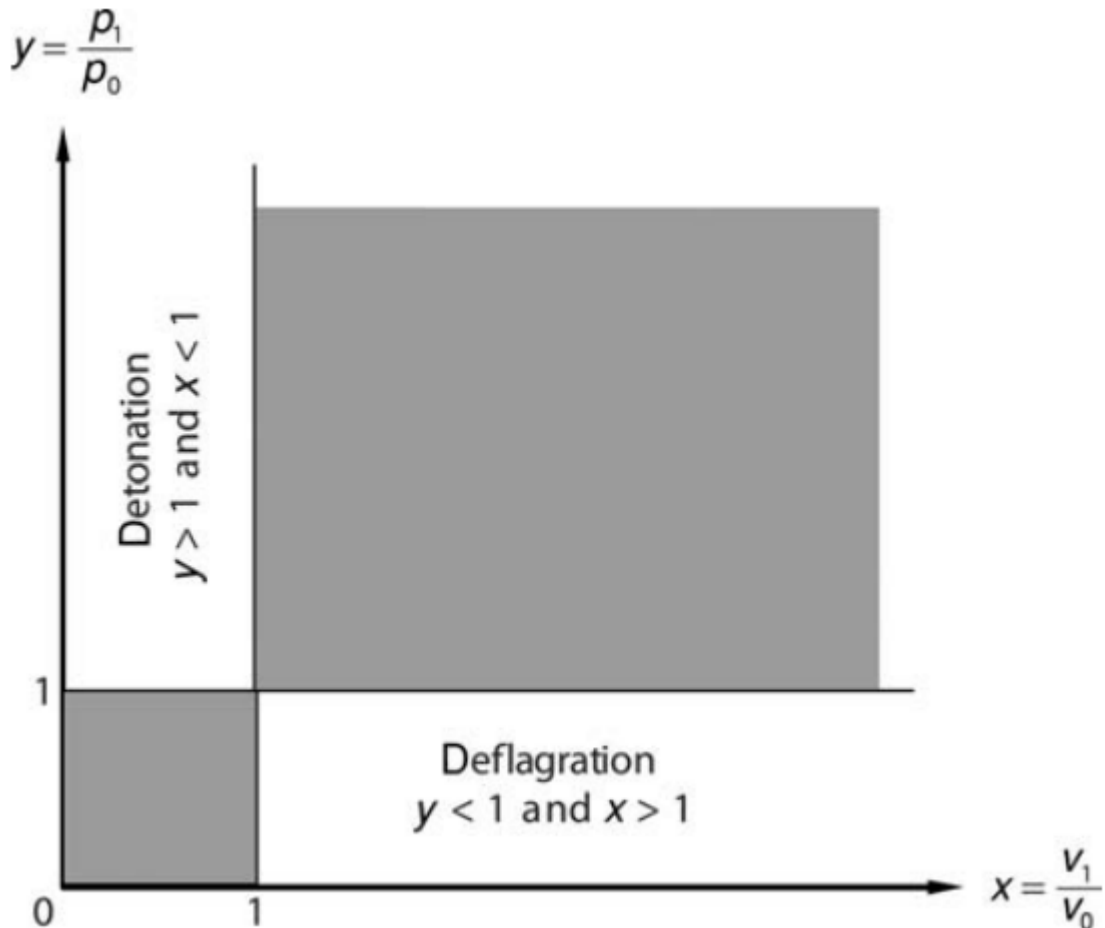
Figure 1.3: Detonation and deflagration domain in the p-v plane (Lee, 2008)

1.2 Motivation

It will be necessary for future terrestrial and interplanetary travel to use strong, controlled methods for high-speed flight and reentry into planetary atmospheres. Reliability of propulsion systems for hypersonic and supersonic flight is crucial for this. We will probably rely on chemical or nuclear propulsion because fuels are readily available for use as propellants. This means that we will need to use a variety of exothermic processes and, consequently, combustion waves. These waves might be

subsonic combustion waves called deflagrations or ultrahigh-speed supersonic combustion waves called detonations. Detonations are a very effective and energetic type of reaction that are typically connected to supernovas and powerful blast explosions. Since detonation-based propulsion systems have the potential to produce more propulsion power than deflagration-based systems, they are now attracting a lot of attention. To fully utilize detonation waves' propulsive potential, we must comprehend their igniting, propagating, and stabilizing properties, which requires our ability to investigate them in a lab environment in addition to through numerical models (Rosato, et al., 2021).

In order to control and harness the reaction power, (Rosato, et al., 2021) presented a novel experimental setup: a hypersonic high-enthalpy reaction facility that creates a detonation that is fixed in space. In a hypersonic flow of hydrogen and air, a standing oblique detonation wave was produced and stabilized on a ramp. Flow diagnostics such as high-speed shadowgraph and chemiluminescence imaging, supported by simulations, demonstrated detonation initiation and stabilization. This advancement in experimental analysis opened up a potential avenue for the development and integration of ultra-high-speed detonation technology, paving the way for hypersonic propulsion and sophisticated power systems.

1.3 Problem Statement

According to UCF researchers, they have successfully confined a continuous explosive detonation, keeping it stationary for the first time. This allowed them to harness its immense energy and convert it into propulsion using a new type of engine called an oblique wave detonation engine. This engine has the potential to achieve speeds up to 17 times the speed of sound, surpassing the scramjet as a hypersonic propulsion technology. Usually, detonations only last for a short period, usually just a few microseconds or milliseconds. However, the team at UCF was able to keep a detonation going for about three seconds through an experimental process until they turned off the fuel. This duration was sufficient to demonstrate that the device was operational. The prototype design is quite similar to what an actual full-scale production Oblique Wave Detonation Engine (OWDE) would resemble. The primary difficulty at present is to understand how to adjust the fuel mix, flow rate, and ramp angle dynamically to

maintain a consistent, dependable, and controllable detonation across a wide range of operating parameters and control inputs (Blain, 2021).

Significant amount of literature is available regarding formation and stabilization of ODWs over a ramp. However, deformation of ramp/wedge structure due to high pressure and temperature and subsequent effects on ODWE combustor performance is not studied. One may suggest usage of stiffer ramps to mitigate such issues. However, such issues still persist since there always exists concerns regarding strength-to-weight ratios in aerospace applications. Hence, this research attempts to study the aero-structural effects on the ramp structure of combustion chamber of an ODWE.

1.4 Objectives of the research

Objectives of the proposed research are illustrated with what follows.

Main Objective

- To study aero-elastic effects of detonation waves on ramp structure of Oblique Detonation Wave Engine (ODWE).

Specific Objectives

- To perform fully-coupled inviscid FSI simulation of a detonative flow field over a compliant ramp structure of an ODWE.
- To perform subsequent FFT analysis of displacement of ramp-tip (solid domain) and movement of induction zone (fluid domain).

CHAPTER TWO: LITERATURE REVIEW

Supersonic combustion finds itself deeply intertwined with the realm of oblique detonation, a combustion mode initiated by an oblique shock wave—a fundamental aspect observed across diverse applications like the ram accelerator and the oblique detonation wave engine. This phenomenon encapsulates a common thread within two-dimensional compressible supersonic reacting flows, constituting an area of substantial research significance and depth. Exploring the domain of supersonic combustion through the lens of oblique detonation prompts critical theoretical inquiries that seamlessly translate into practical quandaries. Questions pertaining to the prerequisites for stable solutions, the dependency of steady propagation speed on the environmental context, the system's vulnerability to instability, and its behavior during periods of unsteady operation emerge as pivotal focal points. Crucially intertwined with these inquiries is the utilization of computational model's adept at accurately describing these complex phenomena—a task central to comprehending the intricacies associated with oblique detonation. The prominence of oblique detonation stems from its pivotal role as the primary combustion process in numerous high-speed propulsion applications, prominently showcased within the ram accelerator—a device representing one such application paradigm. The functionality of the ram accelerator revolves around launching a high-velocity projectile through a light gas gun into a gas-mixture-filled tube, where combustion has not yet commenced, as elucidated by (Powers, 1994). This combustion mode, characterized by oblique shock initiation, serves as a cornerstone across various propulsion contexts, particularly in high-speed propulsion systems like the ram accelerator and the oblique detonation wave engine. Its prevalence within the realm of two-dimensional compressible supersonic reacting flows underscores its profound relevance and extensive research interest, driving critical inquiries into its stable conditions, speed variations, susceptibility to instability, and response to dynamic operational states.

The ability to accurately model these phenomena through computational frameworks stands as an essential pursuit, elucidating the complex dynamics intrinsic to oblique detonation. In particular, the ram accelerator exemplifies the practical manifestation of oblique detonation's significance within high-speed propulsion settings. This device operates by propelling a high-velocity projectile into a gas-filled tube, yet to undergo

reaction, using a light gas gun—a configuration that epitomizes the fundamental combustion process initiated by oblique shock, exemplifying its foundational role in diverse high-speed propulsion mechanisms. The centrality of oblique detonation in the landscape of supersonic combustion extends its reach into pivotal theoretical and practical domains, encompassing the essentiality of stable conditions, the environmental impact on steady propagation, susceptibility to instability, and responses to fluctuating operational dynamics. Accompanying these inquiries is the critical need for computational model's adept at accurately portraying the intricate dynamics intrinsic to oblique detonation—a pursuit crucial for unraveling the complexities embedded within this combustion mode's functionality and relevance within high-speed propulsion paradigms like the ram accelerator and oblique detonation wave engines (Powers, 1994).

(Hertzberg & Bruckner, 2012) conducted an experiment where they observed that when a 70 g projectile was fired into a 16 m long and 38 mm bore tube that was filled with variation combinations of CH_4 (Methane), O_2 (Oxygen), N_2 (Nitrogen), and He (Helium) at a pressure of 31 bar, and then with $0.9\ C_2H_4 + 3\ O_2 + 5CO_2$ at a pressure of 16 bar in the final stage, a shock-induced combustion process occurred. This process caused the projectile to accelerate from an initial velocity of approximately 1,200 m/s to higher velocity of 2,475 m/s (Mach number, M = 8.4) at the end of the tube. Interestingly, the projectile was still accelerating at the end of the tube.

Illustrated within Figure 2.1, the pivotal chemical reaction instigation occurs upon the activation of the initial reflected shock, signifying its paramount significance in this particular context. The association between the temperature-sensitive reaction and the shock wave differs contingent upon the projectile's velocity: swifter projectiles align the temperature-sensitive reaction with the leading shock, while slower-moving projectiles relate it to the succeeding downstream shock. In instances where the projectile's velocity diminishes, the reaction's occurrence is anticipated to shift further downstream within the process. The potential expansion of this apparatus for multiple purposes has been proposed, encompassing its scalability for various applications such as enabling direct launch capabilities into orbit, facilitating investigations focused on impact studies involving hypervelocities, and employing it as a hypersonic test

facility—an idea that has been articulated in the scholarly work by (Hertzberg & Bruckner, 2012).
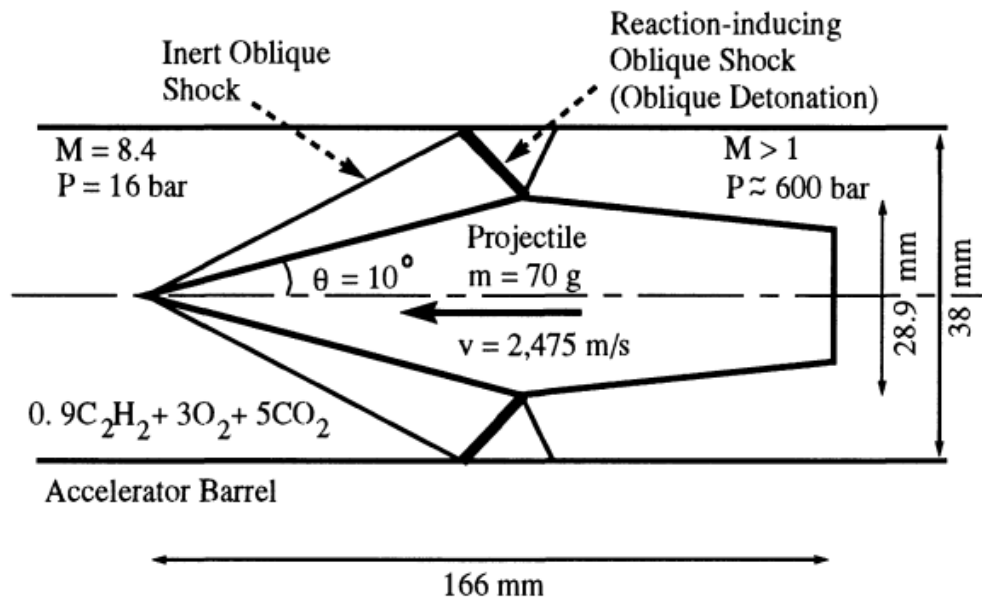
Figure 2.1: Schematic of ram accelerator (Hertzberg & Bruckner, 2012)

The oblique detonation wave engine (ODWE) represents a pertinent propulsion apparatus with a longstanding history in the realm of high-speed aircraft propulsion, as evidenced in the work by (Dunlap & Brehm, 1958). The operational concept of the ODWE, as depicted in Figure 2.2, entails the intake of supersonic air through an inlet while injecting fuel downstream from an onboard source. This mixture encounters a downstream wedge, where the convergence leads to the formation of an oblique shock wave, effectively compressing and igniting the fuel-air amalgam, generating a propulsive force. The ODWE boasts several advantages over conventional air-breathing engines employing subsonic combustion, notably encompassing a simplified design for the supersonic inlet diffuser due to the inherently supersonic nature of the oblique detonation, thus eliminating the necessity for deceleration to subsonic speeds. Additionally, it incurs lower losses in total pressure, requires a shorter combustion chamber length, relies solely on the wedge as the ignition device, and allows for higher flight velocities. Nevertheless, there exist reservations and uncertainties surrounding the ODWE, encompassing aspects such as the absence of static thrust, ambiguities regarding practical mixing lengths, and concerns regarding the stability of the process, as highlighted in (Dunlap & Brehm, 1958).

9

(Dunlap & Brehm, 1958) studied detonation to determine the feasibility of a reaction engine consisting of a combustion chamber that employs a continuous detonation process. Considering hydrogen and acetylene fuels, specific thrust and specific fuel consumption were calculated as functions of flight Mach number. The study concluded an extended speed range of air-breathing engines. Between stations ∞ and 1, supersonic diffusion occurs prior to fuel injection in section 1. Injected fuel is assumed to be fully mixed with air by station 2. Then, detonation occurs at station 3. Immediately downstream of the detonation, conditions at station 4 are assumed to be chemically in equilibrium. Moreover, in the isentropic expansion to atmospheric pressure at the exit, assumption of frozen equilibrium flow conditions is held.
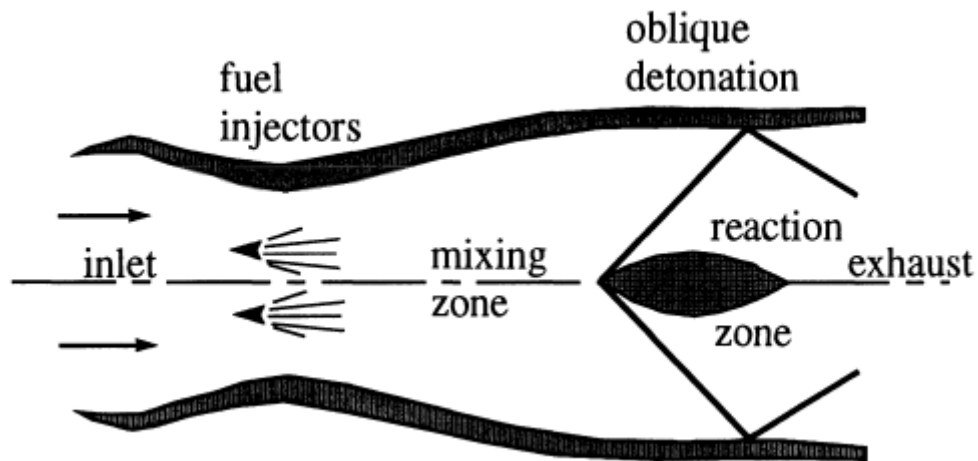
Figure 2.2: Envisioned oblique detonation wave engine (Dunlap & Brehm, 1958)

A typical oblique detonation wave engine integrated into a hypersonic vehicle would look like as shown in Figure 2.3.
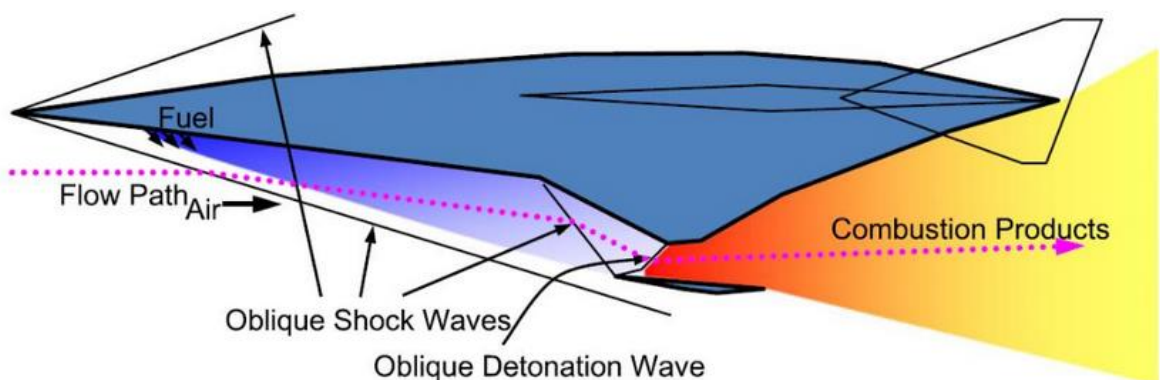
Figure 2.3: A schematic of oblique detonation wave engine (Bulat & Volkov, 2016)

10

For an oblique detonation formed over a ramp, Figure 2.4 shows detailed morphology, specifically showing the induction zone, i.e. the zone/length required for initiation of detonation. Detonation induction length is considered to be the length along the ramp required to form 1% of H_2O formed at the outlet in mass units. Initially, an inert oblique shock is formed which then transitions into an ODW when coupled with reaction front.
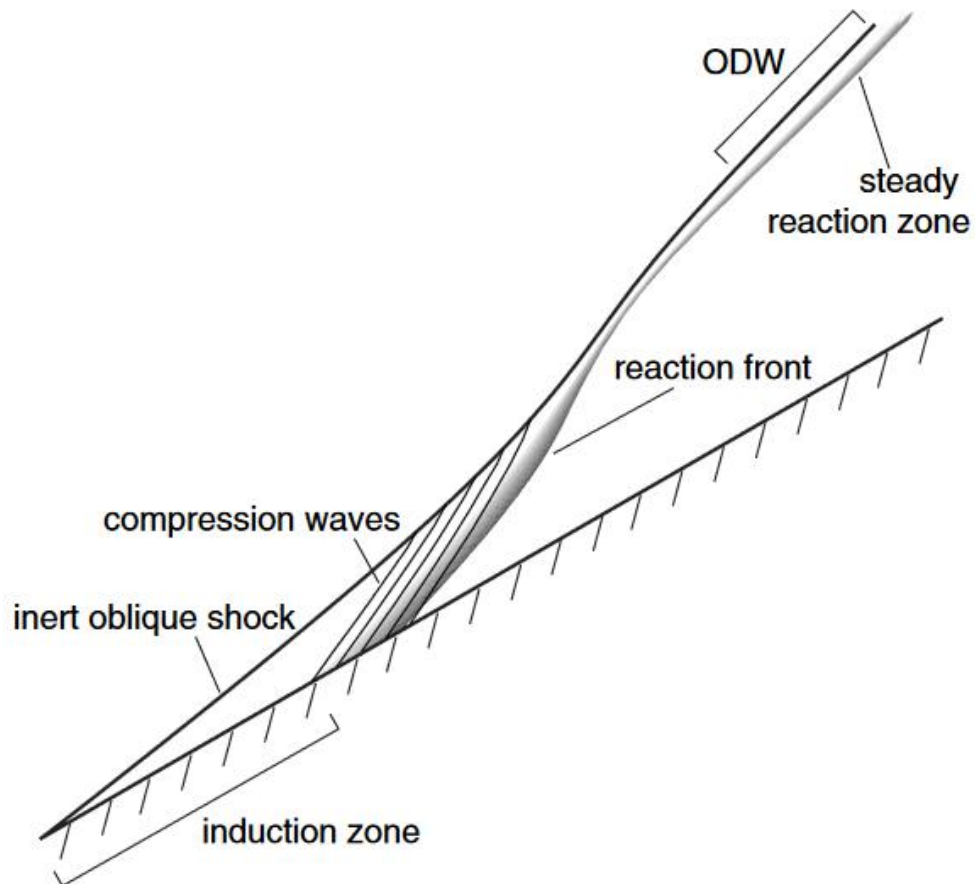
Figure 2.4: Schematic of the formation process of an ODW over a ramp (Verreault, Higgins, & Stowe, 2012)

Normalized temperature, pressure and density when plotted against distance along the ramp show the behavior as shown in Figure 2.5. There exist zone of constant temperature, pressure and density post-inert-shock along which reactions are yet to be initiated. This zone is called induction zone which is then followed by reaction zone where significant reactions happen to increase the temperature of products as well as decrease the pressure and density.
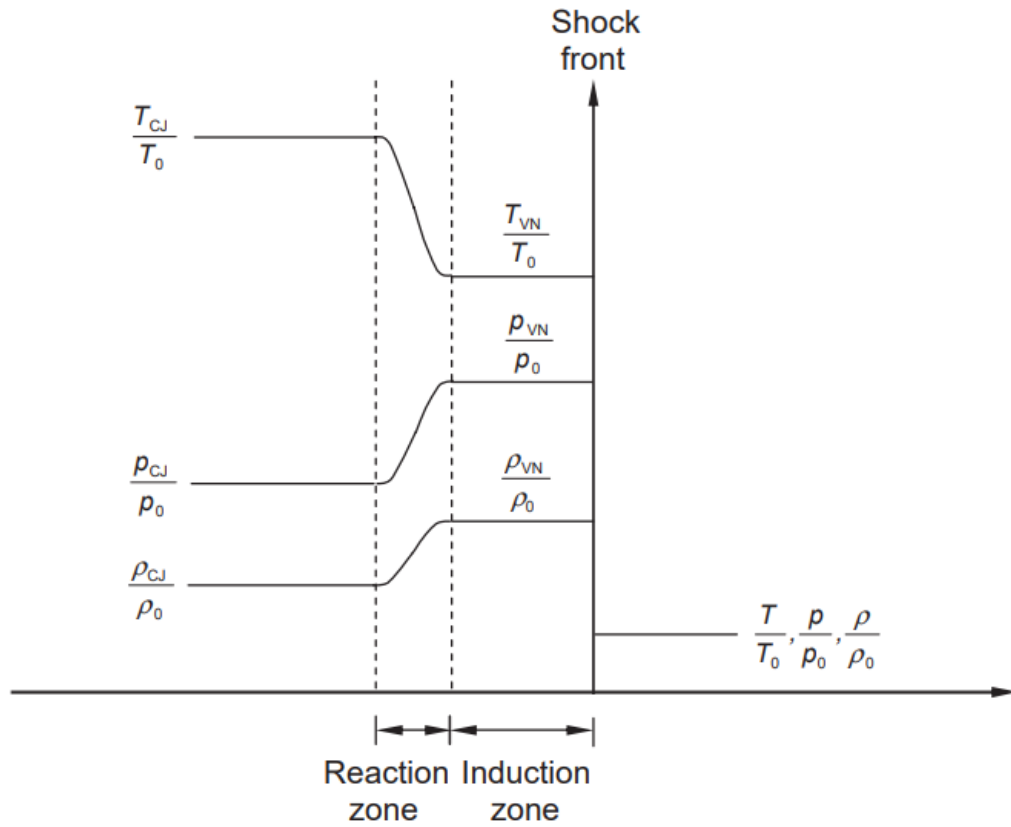
Figure 2.5: ZND model of detonation (Lee, 2008)

Evident in Figure 2.6, at temperatures of 800 K or higher, gas molecules go into vibrational excitation. When temperatures are raised to 2500 K or higher, dissociation of O_2 molecules into O atoms commences, and at temperatures of 4000 K or higher, N_2 molecules start disassociating into N whereas O_2 is almost completely disassociated. Temperature range of 2500 K – 9000 K is hence the range of disassociation. When temperatures are further raised, N and O atoms begin to ionize releasing free electrons and hence called range of ionization (Anderson, 2019).
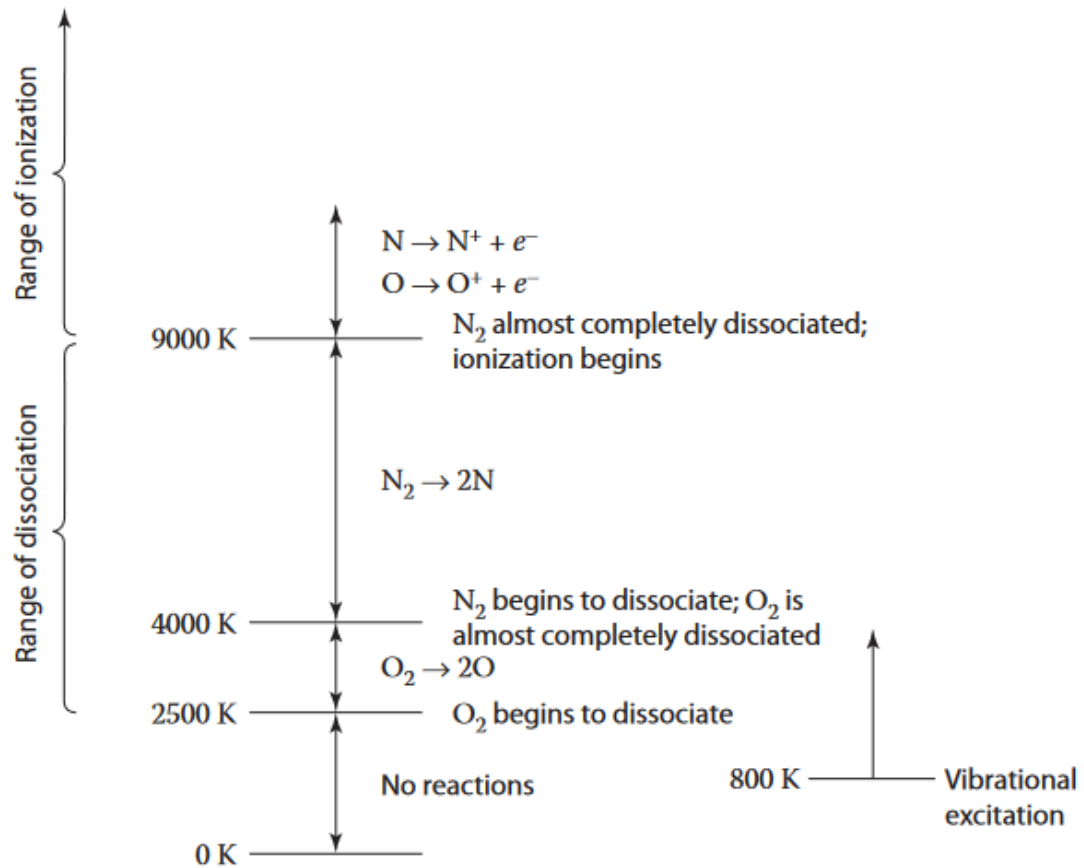
Figure 2.6: Ranges of vibrational excitation, disassociation, and ionization for air at
atmospheric pressure (Anderson, 2019)

Extreme temperatures inducing disassociation should be avoided and hence supersonic
flow needs to be maintained throughout the engine to reduce excessive shock waves
accountable for total pressure losses. Moreover, when properly designed such as the
combustion process occurring after the initiated shock wave is confined to a very short
region, the result is a much shorter combustor and a lighter engine (Dudebout & Sislian,
1998). They numerically simulated hypersonic air-breathing propulsion utilizing
shock-induced combustion ramjets. Euler equations including non-equilibrium
chemical reactions were simulated utilizing lower-upper symmetric Gauss-Seidel
scheme in combination with a symmetric shock-capturing Total Variation Diminishing
(TVD) scheme. 13 species (H_2, O_2, H, O, OH, H_2O, HO_2, H_2O_2, N, NO, HNO, N_2 and
NO_2) finite rate chemistry model with 33 reactions were coupled with Euler equations
and the inviscid reactive flow-field was simulated for 2-dimensional geometries. Their
results indicated shock-induced combustion hold a place as promising technology for
hypersonic propulsion.

An ODE model was constructed by (Zhang, et al., 2022) and the hydrogen-fueled ODE was experimented in a hypersonic wind tunnel. They implemented two theoretical oblique detonations, namely the strong OD mode and weak OD mode at a given wedge angle in the combustor. The study showed no premature inlet combustion and a stable combustion induced by combustor shock waves.

(Hayashi, 2021) considered detonation chamber as a device utilizing tens of kilograms of explosives to destroy chemical warfare materials by detonation. Fragment resistance, operability and leak tightness were satisfied via special structural features. Since instantaneous dynamic pressure is a manifestation of detonation shock wave, application of normal static pressure vessels design code was not a choice. Hence, the study utilized the American Society of Mechanical Engineers' Code Case "Impulsively loaded pressure vessels". To allow detailed design, modes of failure such as fatigue damage and local strain limit were studied using dynamic pressure analysis and dynamic stress-and-strain analysis.

(Hu & Zhang, 2018) developed a fluid-structure coupling method to estimate distribution of parameters in a fluid field accompanied by the combustion of energetic materials. ABAQUS, an engineering simulation software, was used to predict the nonlinear mechanical behaviors. Via a user-defined subroutine interface VUAMP, fluid and structure were coupled through moving boundaries. In order to better understand the effects of the pressure's uneven distribution, parameter distributions in the combustion chamber of a large caliber gun were obtained.

In a laboratory environment, (Xia & Sharkey, 2022) conducted a modeling study involving a small-scale methane/air burner, featuring a bluff body utilized for stabilizing a partially premixed, lean flame characterized by significant oscillations. Within this experimental setup, the burner incorporated a thin steel liner encompassing the combustion chamber, leading to pronounced Fluid-Structure Interactions (FSI) and notable interactions with the airflow and gas dynamics. Employing a combination of computational models including the Flamelet Generated Manifold combustion model, an unsteady RANS (Reynolds-Averaged Navier-Stokes) approach, and the Shear Stress Transport turbulence model, the investigation aimed to predict thermo-acoustic oscillations within the reactive turbulent flow. To handle the complexities arising from structural influences, the study introduced an integrated approach by concurrently

solving structural governing equations alongside the finite volume flow equations computed through Computational Fluid Dynamics (CFD). This integration facilitated a fully coupled, two-way FSI simulation, enabling an accurate prediction of thermo-acoustic instabilities and the consequential solid deformations within the burner. Across various operational conditions investigated, the study revealed that the projected pressure oscillations and wall displacement modes, concerning both frequency and amplitude, closely aligned with the experimental data. Proposing its utility, this approach was suggested as beneficial for the development and anticipation of design and maintenance strategies for gas turbine combustors.

In their work from 2007, (Deiterding & Mauch, 2007) introduced an intricate coupling mechanism involving an Eulerian Cartesian detonation solver infused with dynamic adaptiveness and time-step refinement, which interfaced with a finite element solver integrating a Lagrangian thin shell model equipped with fracture and fragmentation capabilities. The methodology adopted in this approach involved the utilization of a level-set function to effectively represent solid structures on a Cartesian mesh, aiming to synchronize the two distinct solvers for enhanced computational efficiency and a comprehensive understanding of explosive interactions within the context of solid structures. The shell solver mesh was transformed into a distance function using an auxiliary algorithm to efficiently incorporate it into the model. The engineering combustion model eliminated the numerical stiffness inherent to detonation waves, and the approach to modeling fracture was described. The thin-shell solver utilized a subdivision finite element discretization and achieved element separation with interface edges and a cohesive law. To validate the method, the study simulated deformation of a circular thin copper plate under impulsive pressure loading. For a realistic computational application, the study considered a three-dimensional setup in which the passage of an ethylene-oxygen detonation wave induces large plastic deformations and rupture of a thin-walled tubular specimen made of aluminum. Special attention was given to verifying the hydrodynamic loading conditions, and the results of the computational fluid-structure interaction were found to be in agreement with experimental observations.

The utilization of detonation effects on tubes exhibits diverse applications, spanning across domains like oil pipelines and pulse detonation engines. A multitude of

investigations conducted by researchers encompassing experimental, analytical, and numerical methodologies has been aimed at comprehensively unraveling the intricate behaviors of tubes subjected to internal detonation loads, scrutinizing their mechanical, thermo-mechanical, and fracture responses. Within the realm of numerical analyses, a spectrum of techniques comprising interface cohesive elements, mesh-free methods, and extended finite element approaches has been employed to simulate and comprehend the propagation of cracks within these tubes. In a comprehensive review by (Malekan & Khosravi, 2019), an encompassing overview of pertinent literature was presented, synthesizing the landscape of both numerical and experimental analyses delving into the consequential deformation and fracture outcomes stemming from detonation effects on tubes. Their work further encapsulated studies dedicated to the analytical exploration of dynamic loads exerted within detonation tubes, painting a holistic picture of the multifaceted investigations conducted in this intriguing domain.

(Khatir & Pozarlik, 2007) described a study that used numerical methods to investigate how unsteady fluid flow interacts with a vibrating liner in a combustion chamber. The study employed two computational approaches. The first approach involved combining the LES code AVBP, which models combustion, with the FEM code CalculiX, which analyzes structural dynamics. The second approach used the CFD code CFX and the FEM Ansys package. The results of the study, which include applying unsteady fluid structure interaction to a combustion system, were presented and found to be consistent with experimental results.

In processes involving high-speed plate forming and dynamic loading, rapid and substantial deformation occurs within a very brief timeframe. Generating interior shock waves through obstructed channels using gaseous detonation proves to be an effective technique in this context. This method involves the interaction of high-strength pressure waves with a plate, constituting a fundamental mechanism in the forming process. In a study conducted by (Haghgoo & Babaei, 2022), the response of thin steel plates clamped onto triangular frames of varying thicknesses and subjected to different pre-detonation pressures of an acetylene-oxygen mixture was investigated. The primary objective was to assess the permanent deformation patterns of these plates utilizing both experimental and analytical approaches. The research findings revealed that the

16

triangular plate's center of mass underwent the most significant deformation, showcasing substantial plastic deformations in the deflection profiles. To analyze this phenomenon, an energy-based method, originally developed for circular plates, was adapted. Upper limits for the center of mass deformation of the triangular plate were derived by integrating a newly formulated condition. Furthermore, the impact of plate thickness, steel yield strength, and the sizes of the triangular clamps on the plate's displacement was systematically evaluated. Comparing the analytical results with experimental data yielded a strong agreement, emphasizing that thicker plates and slower strain rates led to a considerable reduction in the displacement of the center of mass. The study highlighted that confining gaseous detonation within a truncated conical space can facilitate uniform plate deflection through the interaction of shock waves with the structure. Additionally, the energy-based method proved instrumental in assessing how the limited geometry of the triangular clamp constrained deformation, revealing that the midpoint deflection was hindered by the smaller exposed area of the plate.

Research by (Sourav, Karnick, Singh, & Kartik, 2023) examined the aeroelastic interactions arising from turbulent airflow over a flexible compression ramp. Computational simulations incorporated RANS and URANS fluid models tightly integrated with the linear elastodynamics of the flexible ramp. The primary aim was to gain insights into how aeroelastic phenomena impact shock configuration and movement. During static aeroelastic simulations, alterations in stiffness led to noticeable shifts in shock structure and pressure ratios. Only the most pliable ramp configuration demonstrated flutter instability. Notably, temporal variations in pressure ratios and shock structures were significant. While stiffer ramps remained free from flutter instability, the flexible ramp's oscillations induced oscillatory patterns in shock and pressure along the ramp. These investigations underscore the significance of aeroelastic interplay in the design of supersonic and hypersonic intakes, given the anticipated modifications and interactions of shock structures with the intake cowl.

Sudip Bhattrai's doctoral dissertation, titled "Experimental and numerical study of hypersonic aeroelastic intakes" (Bhattrai, Experimental and numerical study of hypersonic aeroelastic intakes, 2021) undertook a comprehensive exploration into the

complexities of aeroelasticity inherent in off-design scramjet intake operations. This exhaustive investigation was centered on employing a hypersonic wind tunnel to conduct experiments on an aeroelastic intake, with the overarching goal of not only evaluating its performance but also scrutinizing its structural response and the dynamic flow field it engendered. The foundation of this multifaceted study was built upon a series of simulations, including full-scale static 3D models, coupled 2D and 3D aeroelastic simulations, and static 2D simulations, all of which contributed invaluable insights and information pivotal for subsequent experimental setups. The primary objective was to quantify the aeroelastic effects, a feat achieved through meticulous analysis of the dynamic aero-structural response of the intake and its resultant performance, predominantly manifested in the form of the loss of total pressure. The research further delved into an exploration of the evolution of shock wave-boundary layer interaction within the isolator by employing advanced experimental flow visualization techniques. Various methodologies, such as schlieren flow visualization, pressure-sensitive paints, pressure transducers, image tracking from schlieren, and digital image correlation, were employed to measure distinct properties of the flowfield and capture the induced dynamic structural changes. One of the pivotal findings underscored a robust correlation between the deformation of the intake and the resultant overall pressure loss within the isolator. Remarkably, it was observed that a 4% dynamic deformation of the intake's leading edge, normalized concerning its deforming surface length, accounted for fluctuations of up to 36% in total pressure. Intriguingly, in contrast, a 4% static leading-edge deformation, as per the computational fluid dynamics (CFD) solution, resulted in a 37% loss of total pressure. Additionally, the study brought to light phase shifts in the dynamic flow-field response to deformation, contributing to an escalated level of uncertainty concerning practical intake performance. The intricate relationship between the flow-field response, deformation, isolator shock, and boundary layer characteristics was scrutinized, revealing a direct or inverse proportionality based on specific conditions. It was explicitly emphasized that the development, expansion, and movement of recirculation regions inside the isolator emerged as the most crucial factor significantly influencing the intake's flow-field response, overall performance, and the onset of unstart characteristics.

Sudip Bhattrai (Bhattrai S. , McQuellin, Currao, Neely, & Buttsworth, 2021) used basic geometry and structural boundary conditions to conduct an experimental investigation

into the behavior and performance of an aeroelastic hypersonic intake. The tests were carried out at Mach 5.85 in a hypersonic wind tunnel. The compression ramp, which was designed to resemble a cantilever surface in order to replicate the intake's overall deformation, was the most significant deforming element. Pressure transducers, PSPs, and Schlieren flow visualization were used to measure the flowfield. Both feature tracking from the Schlieren videos and digital image correlation were used to measure the dynamic structural response. To measure the impact of intake ramp deformation on intake performance, a pitot tube was used to take a point measurement of the total pressure in the isolator. It was discovered that there was a direct transient correlation between the peak ramp deformation and the loss of total pressure in the isolator, as well as a direct correlation between the intake ramp deformation and the loss of total pressure. The cantilever compliant ramp experienced a 20% reduction in total pressure recovery compared to baseline values during aeroelastic deformation. The analysis demonstrated a strong coupling between the intake structural deformation and the shock-wave/boundary-layer flowfield in the isolator, as well as hysteresis in the dynamic response.

A study (Currao, Bhattrai, & Neely, 2020) encompassed a comprehensive numerical analysis focused on a two-dimensional hypersonic intake operating specifically at Mach 5.85, aimed at discerning aeroelastic oscillations and the consequential thermal degradation of mechanical properties. This study constituted an initial rendition of a wind tunnel experiment, albeit of limited duration, wherein realistic freestream conditions were meticulously applied to extrapolate and simulate the anticipated in-flight behavioral patterns. In this analysis, the exterior of the intake system was meticulously modeled as a cantilevered plate, intended to exhibit free oscillations, strategically designed to simulate the intake's real-world compliance dynamics. The compliance-induced loss in pressure recovery significantly impacted the overall propulsive performance of the vehicle under scrutiny, marking a noteworthy consequence of the observed aeroelastic behavior. Leveraging low-fidelity two-way aeroelastic predictions, the researchers augmented their insights through the assimilation of data garnered from steady-state Reynolds-averaged Navier-Stokes (RANS) simulations. A crucial component of this investigation lay in the iterative process, where the deformed shapes and the distribution of wall temperatures, observed as a consequence of aeroelastic effects, were systematically reintroduced into the

numerical solver. Consequently, it was observed that the pressure loading caused the intake system to undergo a maximum deflection at its leading edge, reaching an approximate magnitude of 2%, resulting in an estimated loss of pressure recovery amounting to approximately 8% based on the findings. Further detailed scrutiny and analysis uncovered an additional cumulative loss of approximately 4% in the pressure recovery metrics, directly attributed to the structural deformations triggered by the consequential deterioration of the material properties. This meticulous examination and analysis underscored the intricate interplay between aeroelastic effects, thermal degradation, and material properties, shedding light on their collective impact on the hypersonic intake's performance.

The research conducted by (Bhattrai S. , McQuellin, Currao, Neely, & Buttsworth, 2018) focused on investigating both rigid and flexible control flaps tailored for hypersonic applications, specifically examining their fluid-structure interaction (FSI) through numerical simulations and experimental methodologies. The primary emphasis lay in managing a trailing-edge flap model undergoing FSI, aiming to evaluate experimental techniques facilitating the assessment of flight control systems in executing hypersonic ground tests. The experimentation involved manipulating test angles for two types of flaps—rigid and compliant—each possessing a 1 mm thickness, ranging from 0° to 20°. These experiments were carried out at the University of Southern Queensland's hypersonic wind tunnel facility (TUSQ), operating under specific flow conditions defined by a Mach number (M) of 5.8, a Temperature (T) of 75 K, and a Pressure (p) of 755 Pa. Simultaneously, numerical simulations were conducted employing US3D, facilitating analyses of 2D and 3D flow fields. To comprehensively gauge the forces and moments acting upon the developed models—specifically lift, drag, and pitching moment—a six-component load cell was utilized, enabling precise measurements. Tests were executed both with and without the load cell to discern the models' individual responses. Flow visualization was facilitated using the schlieren method, offering insights into the flow fields, while the schlieren images were employed to deduce the flap's deformation profile and the response of its trailing-edge oscillations. This investigation uncovered a distinct low-frequency response exhibited by the load cell. In scenarios where the load cell was absent, the flexible flap's trailing-edge oscillations induced a novel structural vibration mode, leading to destructive interference in its oscillation. However, owing to the load cell's low rigidity,

its presence attenuated this vibration, minimizing its detrimental effects. The study's insights and analyses paved the way for envisioning future experiments designed to integrate a software-in-the-loop actuated methodology. This envisioned approach aimed to facilitate control over both rigid and flexible flap models, leveraging the knowledge and data gleaned from this investigation.

CHAPTER THREE: RESEARCH METHODOLOGY

The overall methodology of the current study consists of various stages as shown in Figure 3.1.
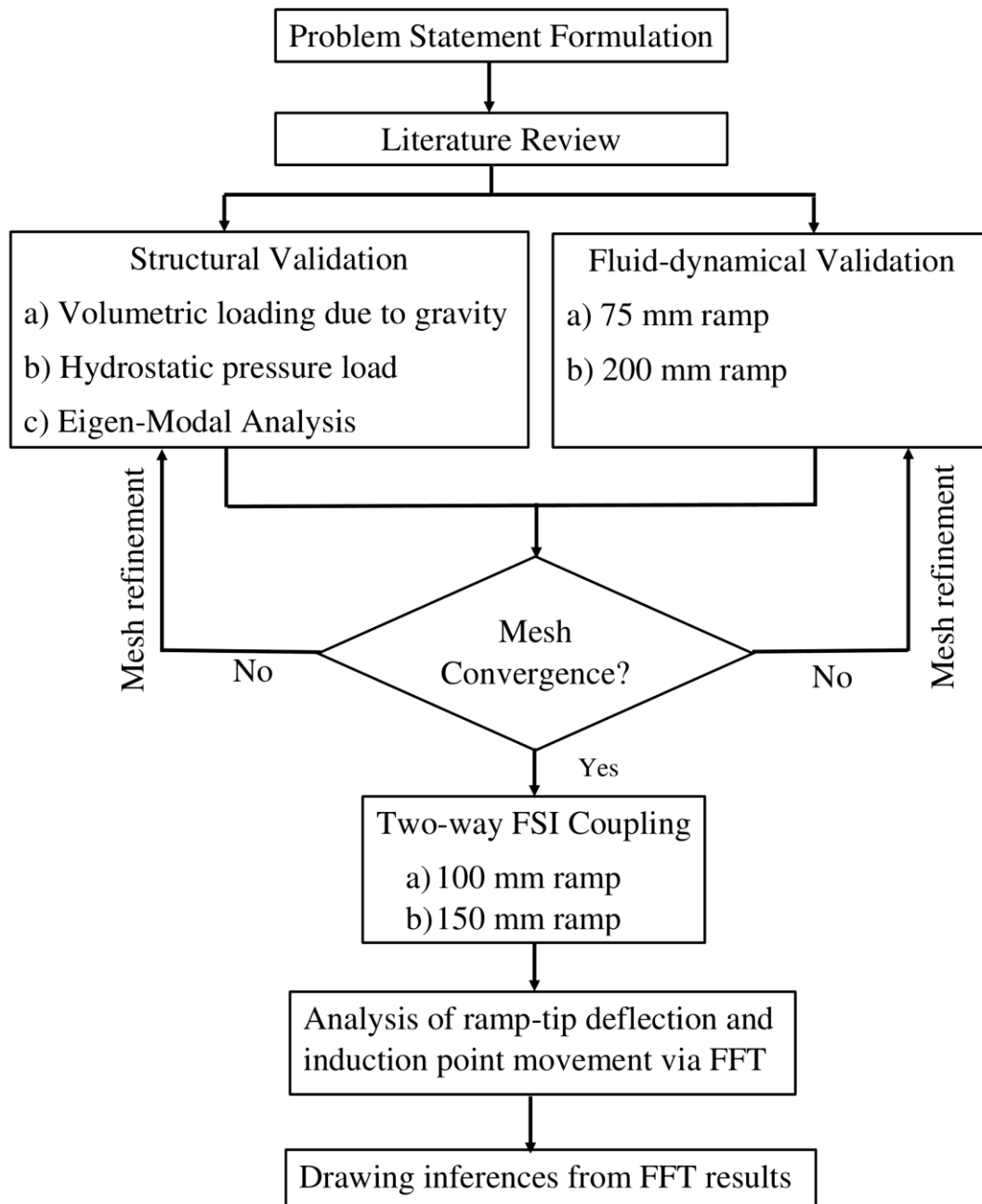
Figure 3.1: Flowchart depicting research methodology

3.1 Problem Statement Formulation

Initially, various research problems were queried with faculty members concerning their research area. Secondly, research arena was narrowed down to aeroelastic simulations in detonative flows motivated by personal interest in aerothermodynamics and fluid-structure interaction. The problem was thereafter reviewed to properly formulate research problem and hence prepare and present a proposal to the faculty members.

3.2 Literature Review

Extensive literature review was conducted so as to build a foundational understanding of various mathematical models/governing equations, numerical techniques and simulation software: OpenFOAM, Calculix and preCICE in this case. Various sources such as textbooks, journal articles, conference papers, review papers and software's user guides as well as tutorials were thoroughly studied to successfully conduct the research.

3.3 Structural Validation

Calculix, an open-source three-dimensional structural finite element program, was utilized for structural side of the FSI simulations. The solver was selected since it possesses capabilities of performing linear as well as non-linear calculations for static, dynamic and thermal problems. Preprocessing required for preparing the geometry and input files (mesh and boundary conditions) to Calculix's number cruncher Calculix-ccx were prepared in Gmsh.

Validation of methodology used for structural side of the FSI simulations consisted of following steps.

3.3.1 Validation via static structural analysis of a cantilever beam subjected to volumetric loading

A cantilever beam as shown in Figure 3.2 of length L (in x-direction) = 350 mm = 35 cm = 0.35 m, width w (in z-direction) = 10 mm = 1 cm = 0.01 m and height h (in y-direction) = 20 mm = 2 cm = 0.02 m was loaded with body force of $\vec{g} = -2\vec{j}$ m/s^2.
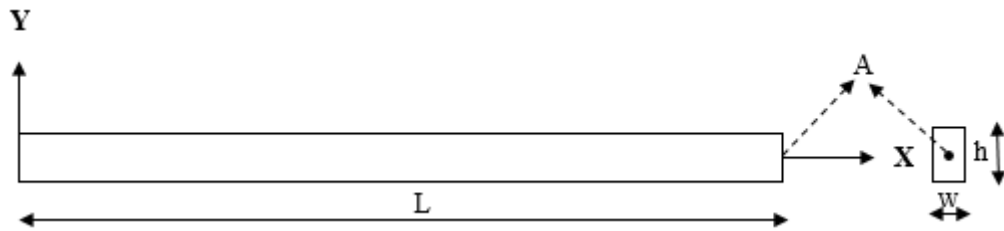
Figure 3.2: Schematic of cantilever beam fixed at left end

Here,

Moment of Inertia (MOI) about z-axis, $I_z = \frac{wh^3}{12} = \frac{0.01*0.02^3}{12} = 6.6665E - 9 \ m^4$

Modulus of Elasticity of the solid E = 1.4E6 N/m^2

Density of solid used ρ = 1000 kg/m^3

Taking point, A as reference point, x and y-displacements of point A were obtained as shown in Table 3.1.

Table 3.1: Mesh independence of static-structural analysis of cantilever beam subjected to gravity load using C3D8 elements

Mesh No.	Mesh Spacing (mm)	$(n_x, \ n_y)$ with $n_z = 2$	No. of cells	$\delta_A X$ (mm)	$\delta_A Y$ (mm)	Relative %Error in $\delta_A Y$
1	10	(35, 2)	70	-4.37994	-51.6219	15.72
2	5	(70, 4)	280	-6.18283	-61.2513	4.84
3	2.5	(140, 8)	1120	-6.83135	-64.3699	1.33
4	1.25	(280, 16)	4480	-7.0167	-65.2385	0.36
5	0.625	(560, 32)	17920	-7.06712	-65.4748	0.10
6	0.3125	(1120, 64)	71680	-7.08103	-65.5406	-

y-displacement of point A as tabulated in Table 3.1 is plotted with mesh spacing (equivalently number of cells) and $_A^\delta Y$ in x and y-axes respectively as shown in Figure 3.3.
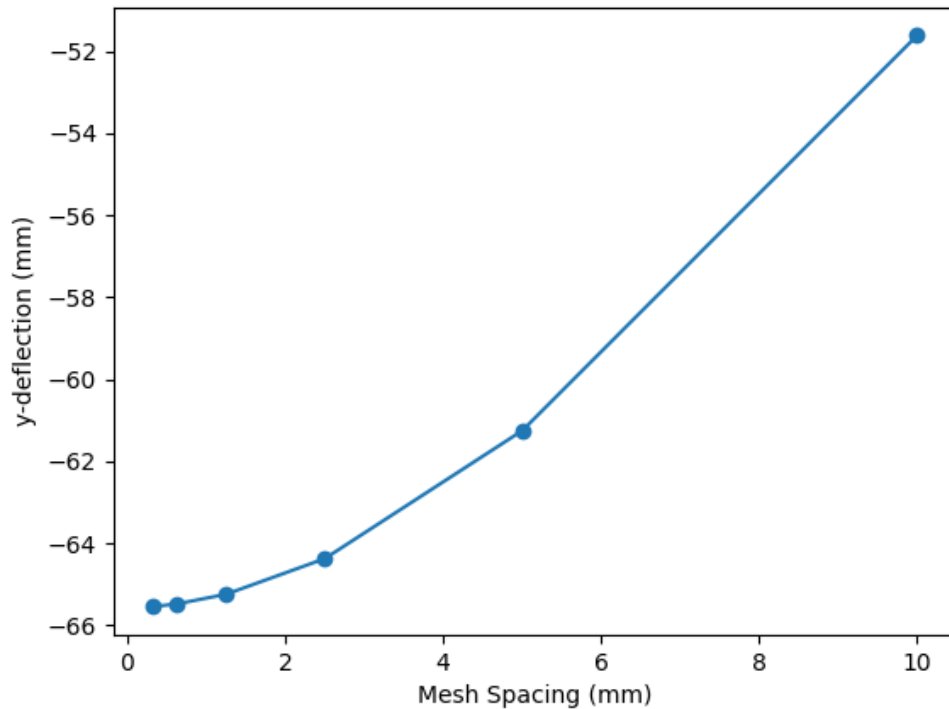
Figure 3.3: y-deflection v/s mesh spacing for cantilever beam subjected to volumetric loading

Findings

When a structure is subjected to volumetric loading (body forces), for instance, gravity loading, Calculix produces results that were independent of width (dimension in Z-direction). This is in accordance with the physical understanding: Stiffness and weight (load on the beam) of the beam increases linearly with width of a homogeneous beam that dictates identical deformation due to self-weight for a beam of any arbitrary width.

The same is true with number of cells along the width of the beam with all other parameters fixed. Identical deformations were obtained for simulation runs with arbitrarily different number of cells in the Z-direction. This is due to the fact that weight of the beam gets uniformly distributed and applied over to the uniformly spaced nodes along the width of the beam.

3.3.2 Static FSI analysis of a cantilever beam subjected to uniform hydro-static pressure load

A cantilever beam of dimensions: Length (L) = 200 mm = 20 cm = 0.2 m, thickness (t) = 10 mm = 1 cm = 0.01 m and width (w) = 1 mm = 0.1 cm = 0.001 m was created and discretized in Gmsh. Some of its parameters are mentioned below:

- Moment of Inertia about z-axis, $I_z = \frac{wt^3}{12} = \frac{0.001 * 0.01^3}{12} = 8.3333e - 11\ m^4$

- Modulus of Elasticity, E = 52.7e9 N/m^2

- Density of solid used, ρ = 2668.75 kg/m^3

- Poisson's ratio, ν = 0.33

- Hydrostatic pressure load applied (p) = 1e6 N/m^2

- Interface area on which pressure p is applied (A) = l*w = 0.2*0.001 = 2e-4 m^2

- UDL applied (w) = p.A/L = 1e6*2e-4/0.2 = 1e3 N/m

- Deflection according to analytical expression $= \delta_{y_{max}} = \frac{wl^4}{8EI} = \frac{1e3 * 0.2^4}{8 * 52.7e9 * 8.3333e - 11} = 4.554098e - 2\ m = 4.554098\ cm = 45.54098\ mm.$

An .inp file was exported which comprises all the information of geometry and the mesh.

The validation methodology for surface loads consisted of following steps:

Step 1] An OpenFOAM case for an inviscid flow over a flat plate was setup with internal field consisting of pressure value = 1e6 N/m^2. This is the same pressure (Uniformly Distributed Load) as that required to be imparted on the surface of cantilever beam.

Step 2] As a part of validation strategy for pressure transfer, the following was done. So as to ensure the required pressure load gets imparted onto the beam surface, i.e. FSI interface, the fluid simulation was run for a significantly small single time step of 1e-15 seconds and then stopped to impose the obtained pressure field (identical to the required pressure) on the FSI interface, i.e. the upper surface of cantilever beam.

Step 3] Next, a static step was performed on the beam to obtain the tip deflection. This was performed without enforcing 2D behavior and with width of the beam 1 mm comprising of a single cell.

Results of calculations for mesh independence analysis performed using above steps are as reported in Table 3.2.

Table 3.2: Mesh independence of static-structural analysis of cantilever beam subjected to uniform hydrostatic pressure load

Mesh No.:	Mesh Spacing (mm)	(n_x, n_y), $n_z = 1$	# of cells	$\delta_{x,3D}$ (m) (-x)	$\delta_{y,3D}$ (m) (-y)	Relative % Error in $\delta_{y,3D}$	Calculix Time (s)	Calculix Time Factor
1	10	20, 1	20	1.5817e-3	3.0024e-2	23.97	6.307401	-
2	5	40, 2	80	3.1710e-3	3.9494e-2	9.70	6.340565	1.005
3	2	100, 5	500	4.0540e-3	4.3740e-2	1.65	6.476869	1.021
4	1	200, 10	2000	4.2169e-3	4.4476e-2	0.15	8.560338	1.321
5	0.5	400, 20	8000	4.2319e-3	4.4547e-2	0.42	13.105387	1.531
6	0.25	800, 40	32000	4.2750e-3	4.4737e-2	0.03	35.766830	2.729
7	0.125	1600, 80	128000	4.2784e-3	4.4753e-2	-	256.761053	7.178

Reference point: Mid-point of top-edge of right face

Mesh independence as well as required Calculix time in seconds are plotted as shown in

Figure 3.4 and Figure 3.5.
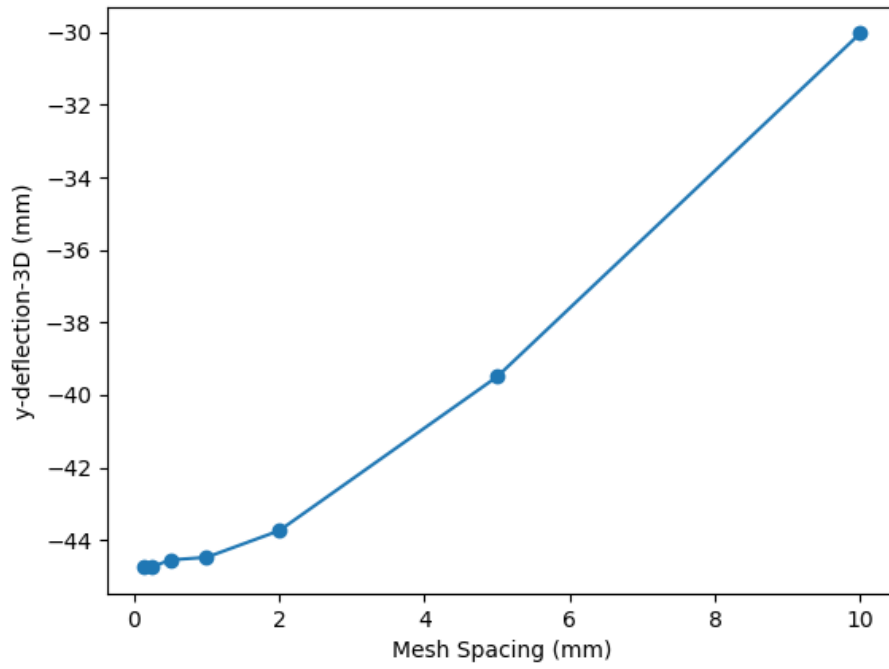
Figure 3.4: y-deflection-3D versus mesh spacing: uniform hydrostatic load
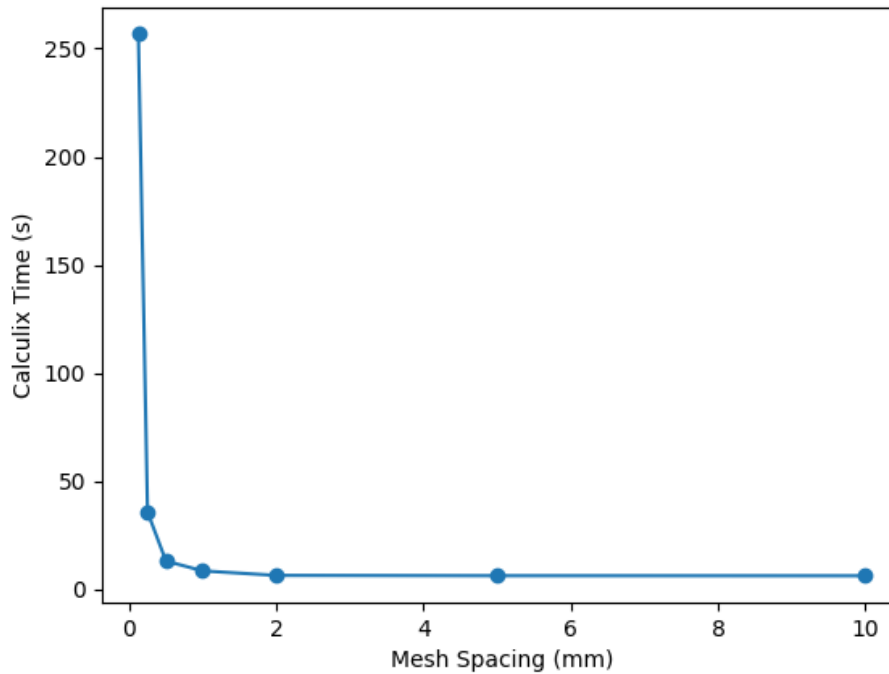
Figure 3.5: Calculix run time versus mesh spacing: uniform hydrostatic load

<u>Finding 1</u>

Accurate (similar to analytical solution) deflections were predicted only when the dimension in the z-direction is made small, for example 1 mm and when nodes were not constrained in the z-direction.

<u>Finding 2</u>

When all the nodes were constrained to move only in the x-y plane, deformations showed drastically different numerals (deformation decreases). Also, calculation time decreases. For instance, for mesh no. 1, $\delta_{x,2D}$ = -8.9953e-04 compared to $\delta_{x,3D}$ = -1.5817e-3 and $\delta_{y,2D}$ = -2.4522e-02 compared to $\delta_{y,3D}$ = -3.0024e-2 with Calculix time = 6.146779 s. Also, for instance, for mesh no. 7, $\delta_{x,2D}$ = -3.2862e-03 compared to $\delta_{x,3D}$ = 4.2784e-3 and $\delta_{y,2D}$ = -4.0109e-02 compared to $\delta_{y,3D}$ = 4.4753e-2 with Calculix time = 95.196360 s.

<u>Finding 3</u>

Considering accuracy corresponding to relative error < 1%, a mesh size of 1 mm was found to be adequate.

3.3.3 Modal Analysis of Cantilever beam

A cantilever beam of dimensions: Length (L) = 200 mm = 20 cm = 0.2 m, thickness (t) = 10 mm = 1 cm = 0.01 m and width (w) = 100 mm = 10 cm = 0.1 m was created and discretized in Gmsh. It was fixed at one end and modal analysis was conducted to evaluate the first two natural frequencies in bending mode of vibration.

All Calculix simulations below were performed using mesh number 7 in the above section (1600, 80) with single cell along the width of the beam.

Moment of Inertia about z-axis, $I_z = \frac{wt^3}{12} = \frac{0.1 * 0.01^3}{12} = 8.3333e - 9 \ m^4$

Modulus of Elasticity, E = 52.7e9 N/m^2

Density of solid used, ρ = 2668.75 kg/m^3

Poisson's ratio, nu = 0.33

First two natural frequencies (Analytical): 179.46 Hz, 1124.66 Hz

Natural frequencies obtained for various values of width w was obtained and were as tabulated in Table 3.3.

Table 3.3: Eigen-modal analysis of cantilever beam with varying width

Width of cantilever beam w (mm)	(2D constraint applied, $n_z = 1$) (ω_1, ω_2) in Hz	(2D constraint not applied, $n_z = 1$) (ω_1, ω_2) in Hz
100	189.97, 1175.60	189.64, 1173.55
10	189.97, 1175.60	181.98, 1126.95
5	189.97, 1175.60	180.21, 1116.17
1	189.97, 1175.60	179.32, 1110.78
0.125	189.97, 1175.60	179.25, 1110.31

Finding

With value of w decreasing (in 2D not constrained case) from 100 mm to 0.125 mm, number of in-between modes (torsional, lateral) were increased. That means, when the 2D constraint was not applied, one has to solve for a greater number of frequencies to obtain required bending frequency, because number of in-between modes of vibration (torsional, lateral, etc) increased with decreasing w.

3.3.4 Mesh independence of modal analysis of cantilever beam

This section explains the following questions: "What value of w to use?" and "What to use: 2D constrained or not constrained?"

A cantilever beam of dimensions: length L = 200 mm = 20 cm = 0.2 m, width w = 100 mm = 10 cm = 0.1 m, thickness t = 10 mm = 1 cm = 0.01 m was considered for calculation of first two modal frequencies. Z-direction dimension was taken to be w = 100 mm and number of cells along the width = 1.

Moreover, 2-D constraint was also applied so as to obtain only the natural bending frequencies. First two Natural frequencies (Analytical): 179.46 Hz, 1124.66 Hz

Results obtained during mesh independence study of modal analysis of cantilever beam are as tabulated in Table 3.4.

Table 3.4: Mesh independence of modal analysis of cantilever beam

Mesh No.	Mesh Spacing (mm)	$(n_x, n_y), n_z=1$	# of cells	Natural frequencies: ω_1, ω_2	%Change
1	10	20, 1	20	243.97, 1512.04	18.85, 18.87
2	5	40, 2	80	205.28, 1271.97	6.58, 6.69
3	2	100, 5	500	192.60, 1192.17	1.02, 1.04
4	1 (chosen)	200, 10	2000	190.65, 1179.89	0.27 ($< 1\%$), 0.27 ($< 1\%$)
5	0.5	400, 20	8000	190.14, 1176.67	0.07, 0.07
6	0.25	800, 40	32000	190.01, 1175.82	0.02, 0.02
7	0.125	1600, 80	128000	189.97, 1175.59	-

Finding

For dynamic simulations, i.e., to predict response frequencies, a mesh size of 1 mm was hence undertaken in all subsequent simulations conducted during this study.

3.4 Fluid-Dynamical Validation

This section explains the solver used for simulation of fluid domain and the utilized governing equations. Moreover, mesh independence studies are also explained for two cases of 75 mm and 200 mm long ramp.

3.4.1 Description of OpenFOAM solver and governing equations

An OpenFOAM-based solver rhoCentralReactingFoam, which is based on rhoCentralFoam and rhoReactingFoam solvers, was utilized to simulate the reactive flow-field. The solver is capable of evaluating Oblique Detonation Waves (ODWs) characteristics in a ramp geometry – a method of initiating ODWs in an ODWE combustor (Bhattarai & Tang, 2016).

The solver solves a set of two-dimensional inviscid (Euler equations) flow-field for an unsteady compressible reactive flow, the conservation forms of which are as below (Adhikari, Hao, & Bhattrai, 2022):

$$\frac{\partial \rho}{\partial t} + \nabla \cdot \left(\vec{\phi}\right) = 0 \qquad \text{Eq. 3.1}$$

$$\frac{\partial \left(\rho \vec{U}\right)}{\partial t} + \nabla \cdot \left(\vec{\phi}\vec{U}\right) = -\nabla p \qquad \text{Eq. 3.2}$$

$$\frac{\partial (\rho E)}{\partial t} + \nabla \cdot \left(\vec{\phi}H\right) = 0 \qquad \text{Eq. 3.3}$$

$$\frac{\partial (\rho Y_i)}{\partial t} + \nabla \cdot \left(\vec{\phi}Y_i\right) = \dot{x}_i W_i \qquad \text{Eq. 3.4}$$

Here, $E = e + \frac{1}{2}U^2$ is total energy, $H = E + \frac{p}{\rho}$ is the total enthalpy. Various fluxes in the divergence terms of above equations include convective face flux $\vec{\phi} = \rho \vec{U}$, energy density flux $\vec{\phi}H$ and species density flux $\vec{\phi}Y_i$ for each species. Above set of equations are deemed closed-set for numerically solving the inviscid reacting flow field via an equation of state for the perfect gas mixture.

$$P = \rho R T \sum_i \frac{Y_i}{W_i} \qquad \text{Eq. 3.5}$$

Here, Y_i denotes mass fraction of the chemical species i, $\dot{x}_i W_i$ is the reaction source term, W_i and $\dot{x}_i$ representing molecular weight of the species and specie molar production rate respectively.

The rate constants k for each elementary reaction are determined using the Arrhenius law which are then used to calculate the specie molar production rate $\dot{x}_i$.

$$k = A T^\beta \cdot exp\left(\frac{-E}{RT}\right) \qquad \text{Eq. 3.6}$$

For the calculation of thermodynamic properties of chemical species, the 7-coefficient NASA polynomial representation for each of two temperature ranges (200 K to 1000 K and 1000 K to 7000 K) was used (Kee, Rupley, & Miller, 1989).

$$\frac{C_{p,i}}{R} = a_{1,i} + a_{2,i}T + a_{3,i}T^2 + a_{4,i}T^3 + a_{5,i}T^4 \qquad \text{Eq. 3.7}$$

$$\frac{H_i}{RT} = a_{1,i} + \frac{a_{2,i}}{2}T + \frac{a_{3,i}}{3}T^2 + \frac{a_{4,i}}{4}T^3 + \frac{a_{5,i}}{5}T^4 + \frac{a_{6,i}}{T}, \qquad \text{Eq. 3.8}$$

Then, calculation of other thermodynamic properties easily follow in terms of C_p and H. Specific heat at constant volume is given by

$$C_{v,i} = C_{p,i} - R \qquad \text{Eq. 3.9}$$

and internal energy U is given by

$$U_i = H_i - RT \qquad \text{Eq. 3.10}$$

The elementary reaction steps for 9-specie-19-steps reaction mechanism are as listed below in Table 3.5 (Bhattarai & Tang, 2016).

Table 3.5: Hydrogen-Air (O_2+N_2) Reaction Mechanism

Reactions	A	β	E_a
$H_2 + O_2 = HO_2 + H$	1.00e+14	0.00	56e+03
$H + O_2 = OH + O$	2.60e+14	0.00	16.8e+03
$O + H_2 = OH + H$	1.80e+10	1.00	8.9e+03
$OH + H_2 = H_2O + H$	2.20e+13	0.00	5.15e+03
$OH + OH = H_2O + O$	6.30e+12	0.00	1.09e+03
$H + OH + M = H_2O + M$	2.20e+22[a]	-2.00	0.0e+00
$H + H + M = H_2 + M$	6.40e+17[b]	-1.00	0.0e+00
$H + O + M = OH + M$	6.00e+16[c]	-0.60	0.0e+00
$H + O_2 + M = HO_2 + M$	2.10e+15[d]	0.00	-1.0e+03
$O + O + M = O_2 + M$	6.00e+13	0.00	-1.8e+03
$HO_2 + H = OH + OH$	1.40e+14	0.00	1.08e+03
$HO_2 + H = H_2O + O$	1.00e+13	0.00	1.08e+03
$HO_2 + O = O_2 + OH$	1.50e+13	0.00	0.95e+03
$HO_2 + OH = H_2O + O_2$	8.00e+12	0.00	0.0e+00
$HO_2 + HO_2 = H_2O_2 + O_2$	2.00e+12	0.00	0.0e+00
$H + H_2O_2 = H_2 + HO_2$	1.40e+12	0.00	3.6e+03
$O + H_2O_2 = OH + HO_2$	1.40e+13	0.00	6.4e+03
$OH + H_2O_2 = H_2O + HO_2$	6.10e+12	0.00	1.43e+03
$H_2O_2 + M = OH + OH + M$	1.20e+17[e]	0.00	45.5e+03

(Units: cm^3, mol, s, kcal, K)

Third-body efficiencies:

a: f N_2 = 1.0, f H_2O = 6.0

b: f N_2 = 1.0, f H_2 = 2.0, f H_2O = 6.0

c: f N_2 = 1.0, f H_2O = 5.0

d: f N_2 = 1.0, f H_2 = 2.0, f H_2O = 16.0

e: f N_2 = 1.0, f H_2O = 15.0

3.4.2 Mesh independence study for flow over a 21-degree 75 mm ramp

Sanjeev Adhikari (Adhikari S. , 2022) conducted various simulations considering detonations formed over ideally sharp infinitely long wedge as well as blunt-tip infinitely long wedge geometries and was considered as the reference case in current study. The author designed a 21° wedge with 75 mm long horizontal span for a stoichiometric H_2-air mixture such at combustor inlet Ma = 6, T = 650 K and p = 42.6 kPa such that the ODW formed hits the wall with near-to-zero mass spillage as shown in Figure 3.6.
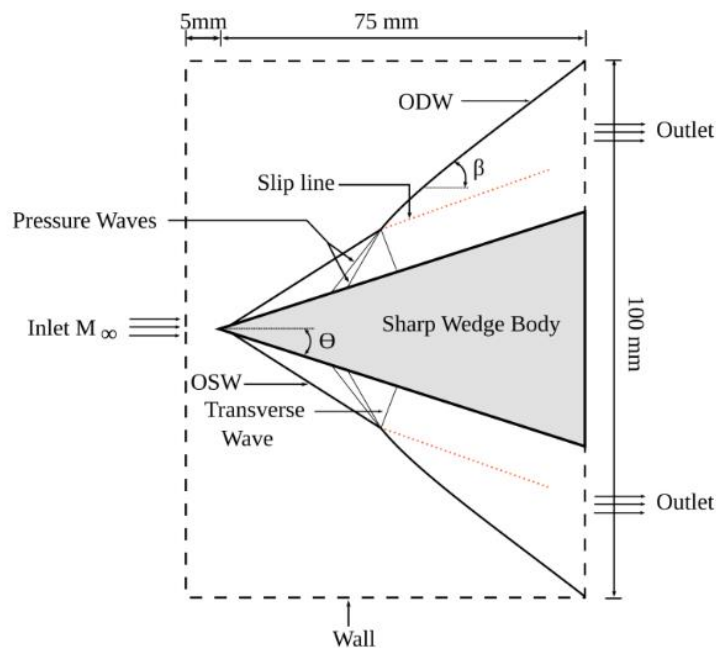

Figure 3.6: Infinitely sharp 75 mm long wedge with near-to-zero mass spillage (Adhikari S. , 2022)

Value of inlet velocity required as the inlet boundary condition needs to be calculated first to initialize at the inlet. It consists of following steps.

Step 1] Calculation of specie mass fraction at inlet

At the inlet,

Equivalence Ratio (ER) = 1

Mixture molar ratio (H₂:O₂:N₂) = 2×ER:1:3.76

Hence,

Mass fraction of H₂ $\quad = Y_{H_2} = \dfrac{2 \times ER \times W_{H_2}}{2 \times ER \times W_{H_2} + 1 \times W_{O_2} + 3.76 \times W_{H_2}}$

$$= \dfrac{2 \times 1 \times 2.01594}{2 \times 1 \times 2.01594 + 1 \times 31.9988 + 3.76 \times 28.0134}$$

$$= 0.02852$$

Mass fraction of O₂ $\quad = Y_{O_2} = \dfrac{1 \times W_{O_2}}{2 \times ER \times W_{H_2} + 1 \times W_{O_2} + 3.76 \times W_{H_2}}$

$$= \dfrac{1 \times 31.9988}{2 \times 1 \times 2.01594 + 1 \times 31.9988 + 3.76 \times 28.0134}$$

$$= 0.22636$$

Mass fraction of N₂ $\quad = Y_{N_2} = \dfrac{3.76 \times W_{N_2}}{2 \times ER \times W_{H_2} + 1 \times W_{O_2} + 3.76 \times W_{H_2}}$

$$= \dfrac{3.76 \times 28.0134}{2 \times 1 \times 2.01594 + 1 \times 31.9988 + 3.76 \times 28.0134}$$

$$= 0.74512$$

where, W_i is gram molecular weight of specie i. We have, $W_{H_2} = 2.01594$, $W_{O_2} = 31.9988$ and $W_{N_2} = 28.0134$.

Initially (at t = 0), the channel was initialized so as to be filled with a premixed mixture.

Step 2] Calculation of cp and cv of mixture

Thermodynamic properties of species were obtained using the NASA's 7-coefficient polynomial representation.

Specific heat at constant pressure of ith species ($C_{p,i}$ in J.mol^{-1}.K^{-1}) was calculated using:

$$\frac{C_{p,i}}{R} = a_{1,i} + a_{2,i}T + a_{3,i}T^2 + a_{4,i}T^3 + a_{5,i}T^4, \qquad R = 8.314\,J.mol^{-1}.K^{-1}$$

Low-temperature C_p coefficients (200 K< T < 1000 K) for H_2, O_2 and N_2 are as listed in Table 3.6 (National Institute of Standards and Technology, 2013).

Table 3.6: Polynomial coefficients for calculating C_p for H_2, O_2 and N_2

Specie	a_1	a_2	a_3	a_4	a_5
H2	3.298124	0.0008249442	-8.143015e-7	-9.475434e-11	4.134872e-13
O2	3.212936	0.001127486	-5.76615e-7	1.313877e-9	-8.768554e-13
N2	3.298677	0.00140824	-3.963222e-6	5.641515e-9	-2.444855e-12

Using above coefficients for the expression of molar C_p, at T = 650 K, we obtain,

C_{p,H_2} = 29.4156261 J.mol^{-1}.K^{-1}

C_{p,O_2} = 32.48199873 J.mol^{-1}.K^{-1}

C_{p,N_2} = 30.36647648 J.mol^{-1}.K^{-1}

Next, on mass units,

$c_{p,H_2} = \dfrac{C_{p,H_2}}{W_{H_2}}$ = 14.59151864 kJ.kg^{-1}.K^{-1}

$c_{p,O_2} = \dfrac{C_{p,O_2}}{W_{O_2}}$ = 1.015100527 kJ.kg^{-1}.K^{-1}

$c_{p,N_2} = \dfrac{C_{p,N_2}}{W_{N_2}}$ = 1.0839998247 kJ.kg^{-1}.K^{-1}

Then, we obtain,

Mean specific heat at constant pressure (in molar units), $\overline{C_p} = \sum_{i=1}^{N} X_i C_{p,i}$

In mass units,

$$\bar{c}_p = \sum_{i=1}^{N} Y_i c_{p,i} = 0.02852 \times 14.59151864 + 0.22636 \times 1.015100527 + 0.74512 \times 1.0839998247 = 1.453638 \text{ kJ.kg}^{-1}.\text{K}^{-1}.$$

Step 3] Calculation of Apparent (mean) molecular weight of the mixture

We have,

$$\bar{W} = \frac{Total\ mass\ of\ mixture}{Total\ no.of\ moles\ in\ mixture}$$

$$= \frac{m_{H_2} + m_{O_2} + m_{N_2}}{N_{H_2} + N_{O_2} + N_{N_2}}$$

$$= \frac{2 \times W_{H_2} + 1 \times W_{O_2} + 3.76 \times W_{N_2}}{2 + 1 + 3.76}$$

$$= X_{H_2} \times W_{H_2} + X_{O_2} \times W_{O_2} + X_{N_2} \times W_{N_2}$$

$$= \frac{2}{2 + 1 + 3.76} W_{H_2} + \frac{1}{2 + 1 + 3.76} W_{O_2} + \frac{3.76}{2 + 1 + 3.76} W_{N_2}$$

$$= 20.9114 \ g/mol$$

Hence, $r_{mix} = \frac{R}{W} = \frac{8.314 \ KJ.kmol^{-1}.K^{-1}}{20.9114 \ kg/kmol} = 0.397582 \ kJ.kg^{-1}K^{-1}$

Now, $\bar{c}_v = \bar{c}_p - r_{mix} = 1.453638 - 0.397582 = 1.056056 \ kJ.kg^{-1}K^{-1}$

Then, $\gamma_{mix} = \frac{\bar{c}_p}{\bar{c}_v} = 1.3765 \ kJ.kg^{-1}K^{-1}$

So, speed of sound in the mixture $a_{mix} = \sqrt{\gamma_{mix} r_{mix} T} = 596.43 \ m/s$

This gives, $V_{inlet} = M a_{mix} = 6 \times 596.43 = 3578.6 \ m/s$

Figure 3.7 shows the schematic of computational domain as well as boundary conditions utilized for both fluid-dynamical and fully-coupled FSI simulations.

| | a) | b) |
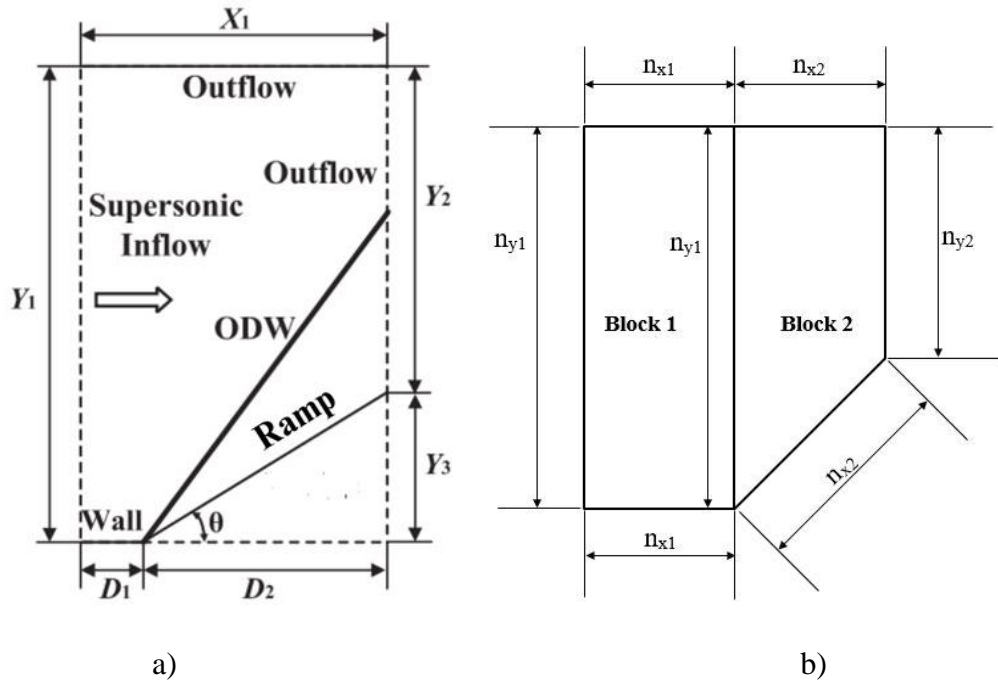
Figure 3.7 (a) Boundary conditions for fluid-domain (b) Multi-block fluid mesh

Utilizing the computational domain shown in Figure 3.7 and for inlet velocity equivalent to Mach 6 for a stoichiometric Hydrogen-Air mixture at T = 650 K, p = 42.6 kPa, various simulations were performed and their results tabulated in Table 3.7.

Table 3.7: Mesh independence study for flow over a 21°, 75 mm ramp

Grid Type	Block wise Cell Count	No. of Cells	T_{max} (K)	Induction Length (mm)
Coarse	Block 1: (5, 50) Block 2: (80, 50)	4250	2930.57	10.04
Medium	Block 1: (10, 100) Block 2: (160, 100)	17000	2940.72	12.05
Fine I	Block 1: (20, 200) Block 2: (320, 200)	68000	2943.67	13.05
Fine II	Block 1: (40, 400) Block 2: (640, 400)	272000	2979.77	13.31

Contours of mass fraction of H_2, mass fraction of H_2O and pressure are as shown in Figure 3.8,

Figure 3.9 and

Figure 3.10 respectively that show the structure of oblique detonation waves over a ramp structure. All contours were obtained using Fine II mesh.
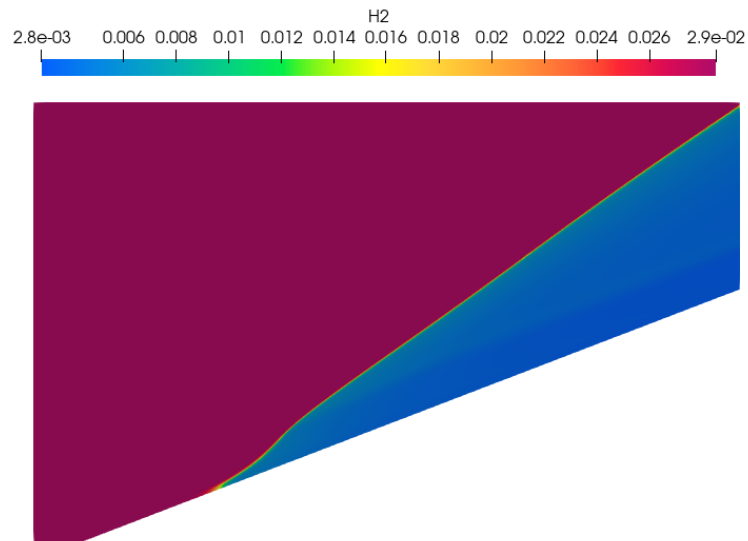

Figure 3.8: H_2 contour showing near-to-zero mass spillage for a 75 mm rigid ramp
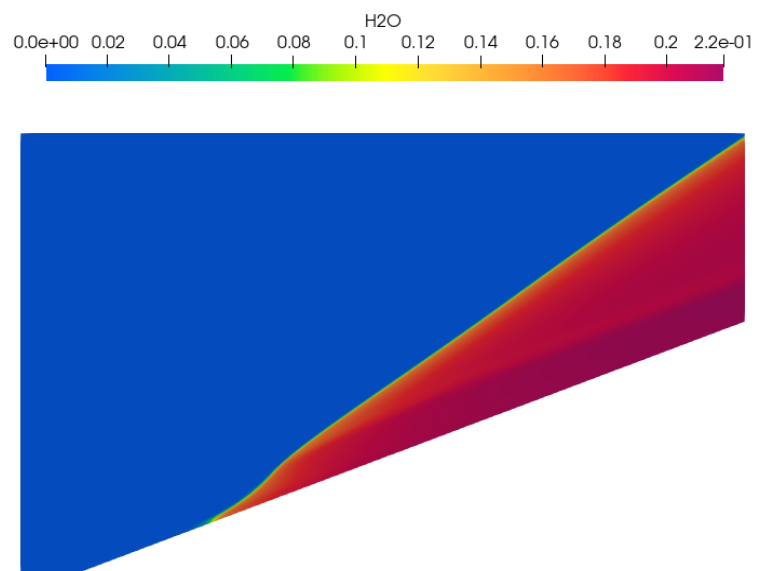
Figure 3.9: H_2O contour showing near-to-complete combustion for a 75 mm rigid ramp
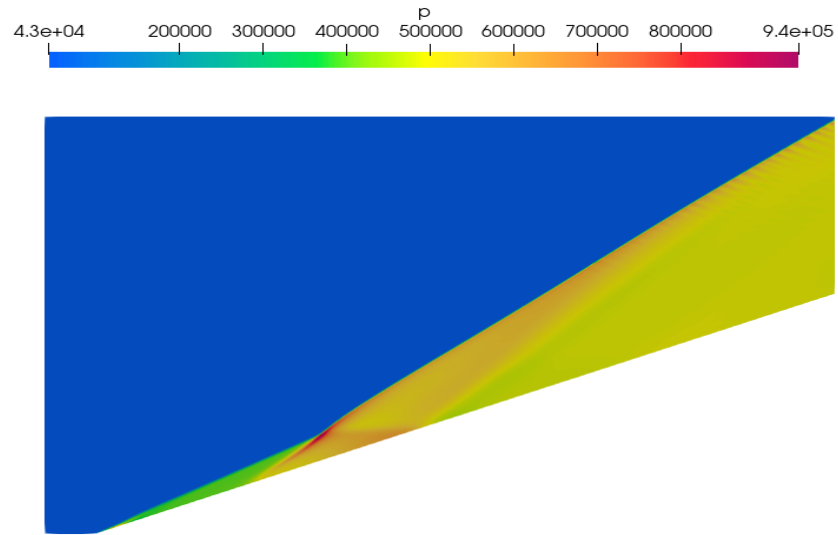
Figure 3.10: Pressure contour showing induction zone and triple point for a 75 mm rigid ramp

3.4.3 Mesh independence study for flow over a 21-degree 200 mm ramp

Utilizing the identical computational domain, various simulations were performed for 200 mm ramp and obtained results were tabulated in Table 3.8.

Table 3.8: Mesh independence for flow over a 21º, 200 mm ramp

Grid Type	Blockwise Cell Count	No. of Cells	T_{max} (K)	Induction Length (mm)
Coarse	Block 1: (5, 133) Block 2: (200, 133)	27265	2939.07	9.64
Medium	Block 1: (7, 187) Block 2: (280, 187)	53669	2944.95	10.71
Fine I	Block 1: (10, 266) Block 2: (400, 266)	109060	2951.39	12.85
Fine II	Block 1: (20, 532) Block 2: (800, 532)	436240	2954.82	13.12

40

3.5 FULLY-COUPLED FSI SIMULATION

All FSI simulations were carried out with Fine I fluid-mesh (Δx = 0.5 mm) for 10 mm thick ramp and extruded a single cell of 1 mm in z-direction. Considering solid mesh, C3D8 brick elements of size 1 mm were used for all subsequent FSI simulations.

3.5.1 Software Used

Some of the major software utilized while performing fully-coupled FSI simulations are as listed and explained below.

(i)   Gmsh: Gmsh is a 3D finite element mesh generator with built-in pre- and post-processing capabilities **(Geuzaine & Remacle, 2009)**. It was used to initially create structured mesh for the solid-part and export as an .inp file for Calculix.

(ii)   Calculix GraphicX: **(Dhondt & Wittig, 2023)** This software was used to create .msh and .nam files for Calculix CrunchiX. This toolkit is quite a powerful yet old-fashioned visualization software. Hence, ParaView was instead used for results visualization and subsequent post-processing.

(iii)   Calculix CrunchiX: (Dhondt & Wittig, 2023) This software was used as the Finite Element solver for simulating structural dynamics. This is the solver counterpart to the visualization software GraphicX. This is the actual number cruncher of Calculix that does the job of computations.

(iv)   OpenFOAM v2112: OpenFOAM stands for Open Source Field Operation and Manipulation. It is a free and open-source CFD software whose primary developer is OpenCFD Ltd since 2004. It covers features that are extensively included but not limited to flows involving chemical reactions, turbulence and heat transfer, acoustics, solid mechanics and electromagnetics (OpenCFD Ltd, 2023). This software was used for the fluid simulation.

(v)   preCICE: preCICE stands for Precise Code Interaction Coupling Environment. It is an open-source coupling library that can handle multi-physics simulation and is built to solve those problems in a partitioned approach. The library supports but is not limited to coupled phenomena such as Fluid Structure Interaction (FSI) and Conjugate Heat Transfer (CHT) (preCICE, 2023).

3.5.2 Limitations of the research

Limitations listed below explain the scope of the research.

Structural simulation

a) Strictly 2D simulations were performed so as to restrict the deformation to planar modes.

b) C3D8 brick elements were used due to their convenience and their prevalence in bending problems as they predict bending deflections well. However, other type of elements that can predict stresses more accurately should be explored when stresses generated are our priorities.

Fluid simulation

a) Inviscid approximations to full NS equations were imposed, i.e. reactive two-dimensional Euler equations were solved.

b) Relatively coarse meshes in fluid domain were used for fully coupled FSI simulations compared to fluid-dynamical simulations due to computationally economic reasons.

CHAPTER FOUR: RESULTS AND DISCUSSION

A freestream flow of stoichiometric H_2-air (O_2 + N_2) mixture with p = 42.6 kPa, T = 650 K and M = 6 was simulated over a 21^0 ramp. These conditions at ER=1 corresponds to a fully combusted mixture with almost zero mass-spillage to the nozzle. Two cases were considered viz, ramps with D_2 = 100 mm and 150 mm. The structure's computational domain is as shown in Figure 4.1.
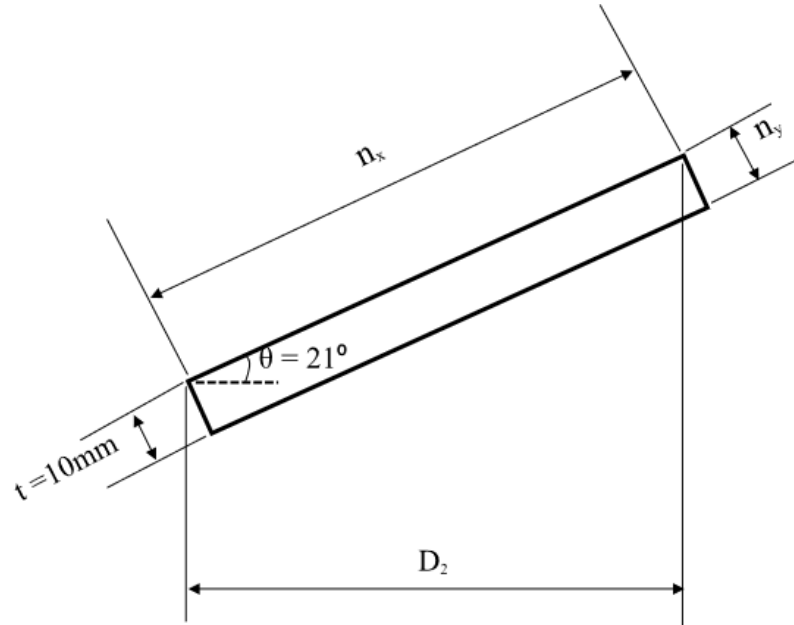
Figure 4.1: A schematic of solid computational domain for the ramp structure

4.1 Case FSI.A] 100 mm ramp

A fluid mesh of (10 x 133) and (216 x 133) in blocks I and II and a solid mesh of (108 x 11) was utilized. This mesh size was chosen after careful consideration of tradeoff between computational accuracy and economy.

Modal frequencies for the 21°, 100 mm ramp were calculated to be ω_1 = 659.54 Hz and ω_2 = 3962.43 Hz. This task was performed in CalculiX. Utilizing the *MODAL keyword, one can perform such calculations to obtain any number of frequencies of interest.

For this case, y-displacement of ramp-tip versus time graph looks like Figure 4.2.
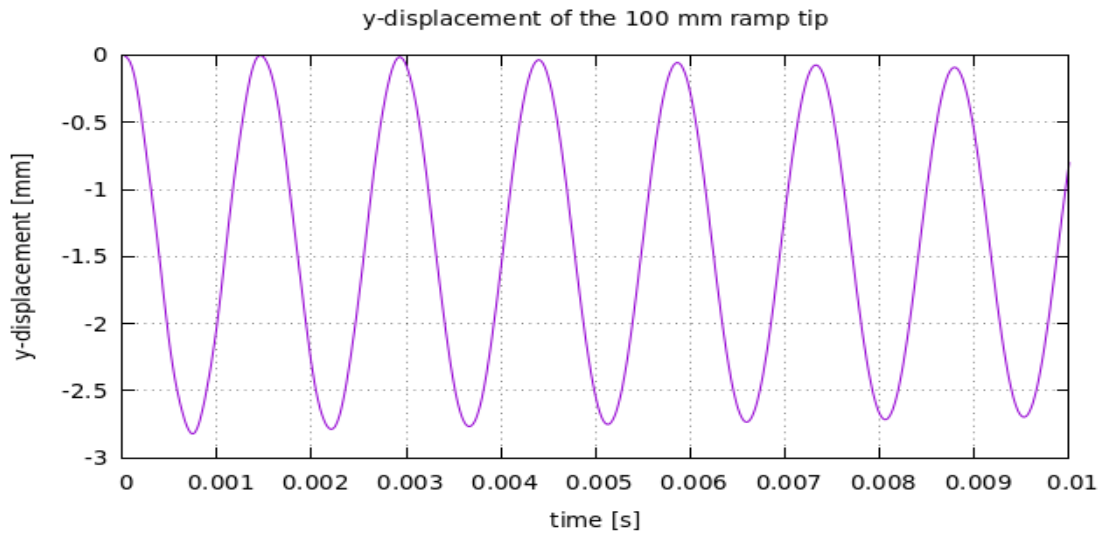
Figure 4.2: Time evolution of y-displacement of the 100 mm ramp-tip

4.1.1 FFT of y-displacement of 100 mm ramp tip

By performing FFT analysis, it was found that the frequency at which maximum amplitude occurs is: 700.0 Hz as shown in Figure 4.3.

Figure 4.3: First-mode dominant response of 100 mm ramp tip

4.1.2 FFT of induction length of 100 mm ramp

By performing FFT on induction length variation versus time, it was found that its movement was first mode dominated with frequency of 600 Hz as seen in Figure 4.4.

Figure 4.4: First-mode dominant movement of induction length for a 100 mm ramp

A plot showing H2 concentration at t = 9e-4 s corresponding to approximately maximum displacement occurring during the oscillation is shown in Figure 4.5 depicting the mass-spillage. This leads to loss in combustion efficiency.
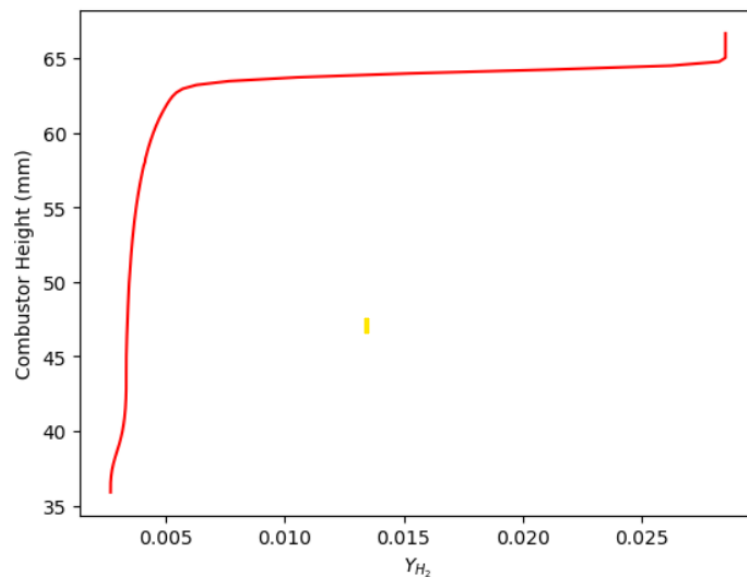
Figure 4.5: Spillage of unburned H_2 into nozzle at t = 0.9 ms for 100 mm ramp

4.2 Case FSI.B] 150 mm

A fluid mesh of (10 x 200) and (320 x 200) in blocks I and II and a solid mesh of (160 x 10) was utilized.

Modal frequencies for the 21°, 150 mm ramp were calculated to be $\omega_1 = 294.10$ Hz and $\omega_2 = 1807.73$ Hz.

For this case, y-displacement of ramp-tip versus time graph looks like Figure 4.6.
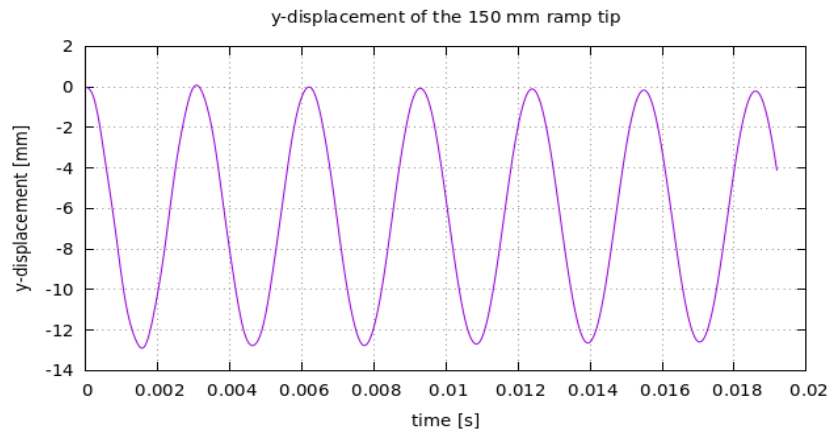
Figure 4.6: Time evolution of y-displacement of the 150 mm ramp-tip

4.2.1 FFT of y-displacement of 150 mm ramp tip

By performing FFT analysis as shown in Figure 4.7, it was found that the frequency at which maximum amplitude occurs is 312.83 Hz.
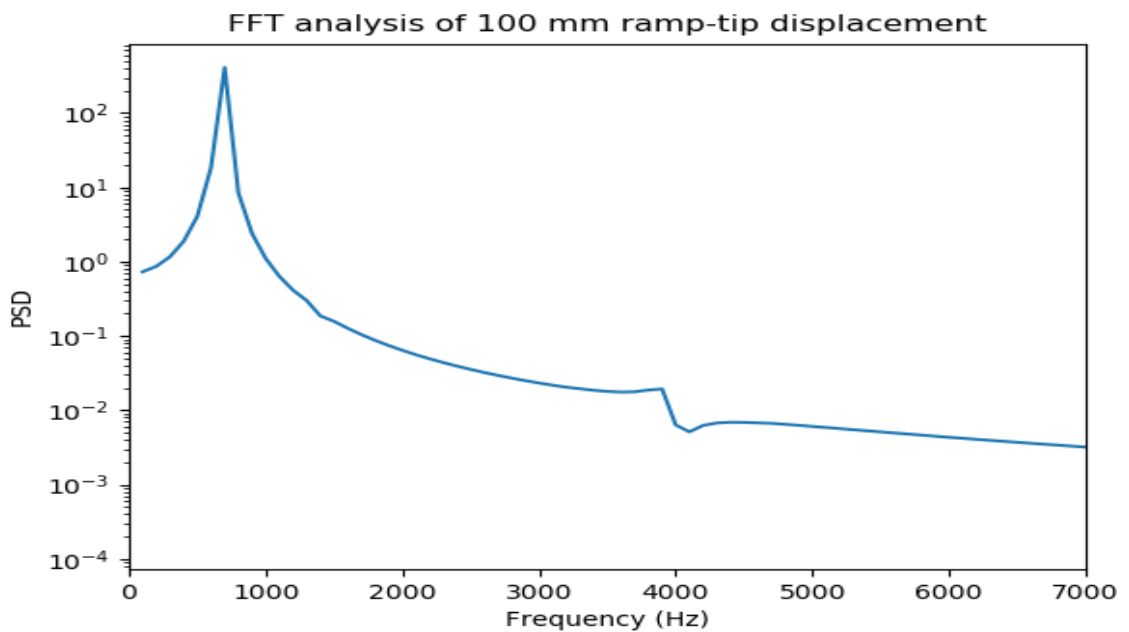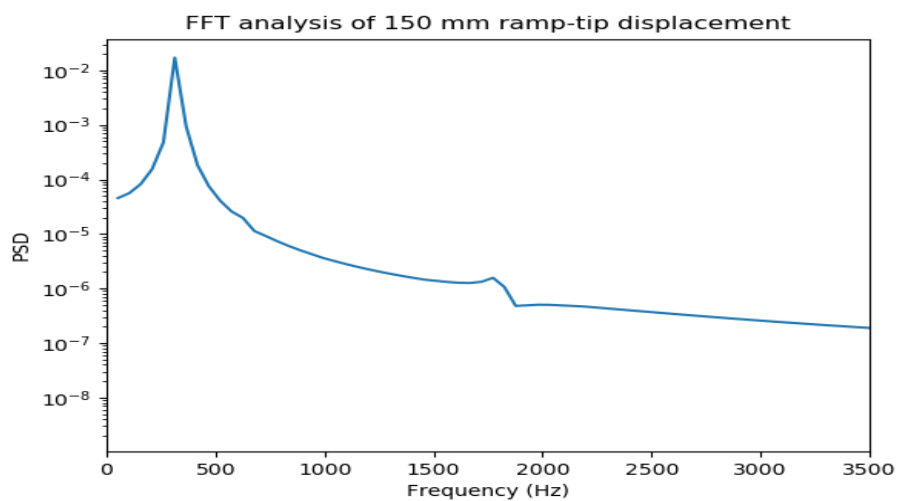

Figure 4.7: First-mode dominant response of 150 mm ramp tip

4.2.2 FFT of induction length of 150 mm ramp

By performing FFT on induction length variation versus time, it was found that its movement was first mode-dominated with frequency of 312.66 Hz as seen in Figure 4.8.
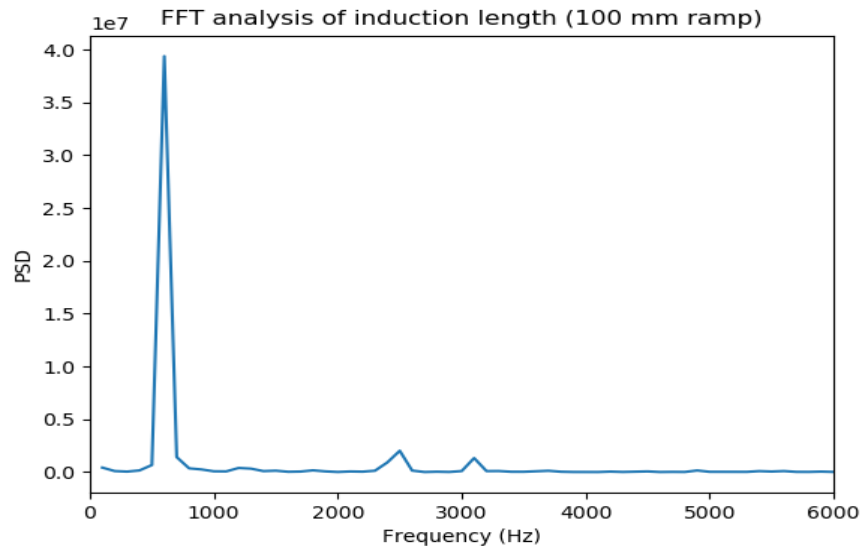

Figure 4.8: First-mode dominant movement of induction length for a 150 mm ramp

CHAPTER FIVE: CONCLUSIONS AND RECOMMENDATIONS

5.1 CONCLUSIONS

Based on tasks performed on the basis of specific objectives, the following conclusions were inferred.

1) Fully-coupled FSI simulations were carried out for a flexible ramp structure of an ODWE at M = 6, p = 42.6 kPa and T = 650 K for a stoichiometric pre-mixed H_2-Air mixture considerin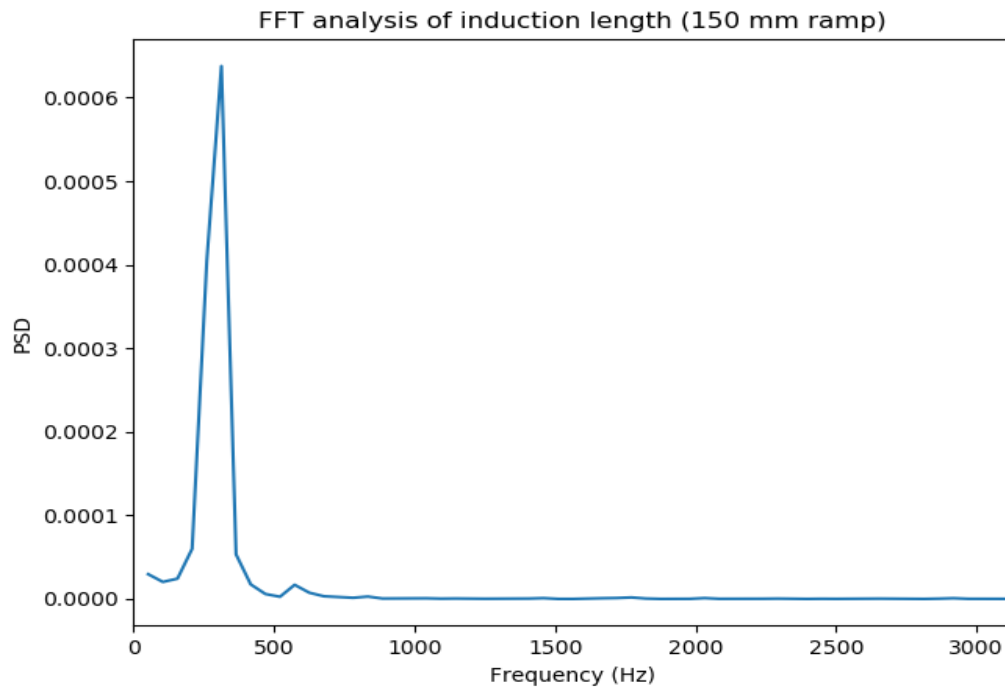g ramps of horizontal span 100 mm and 150 mm. Six cycles of oscillation of ramp-tip were obtained for both cases and were subsequently analyzed via FFT.

2) For 150 mm ramp vibrating at $\omega_{ramp} = 312.8$ Hz, induction zone was found to almost catch up with $\omega_{ind} = 312.6$ Hz whereas for 100 mm ramp vibrating at $\omega_{ramp} = 700$ Hz, induction zone was found to lag behind with $\omega_{ind} = 600$ Hz. The latter indicates that there exists phase difference between structure's displacement and the detonation phenomenon, induction length being the reference parameter of the fluid domain. Results indicated the first-mode dominated response of the ramp structure which in-turn also dictates the first-mode response regarding the movement of induction zone. These results suggest subsequent existence of uncertainties in combustor performance parameters due to aero-elastic effects.

5.2 RECOMMENDATIONS

Outliers were also visible in the unfiltered data sets for the position of induction zone apart from an overall oscillating pattern. This was attributed to relatively coarser grids utilized in the fully-coupled cases. To fully understand the two-way effects of detonation waves on the ramp structure, a moderately-high-density mesh is recommended to be used.

Owing to existence of extremely high temperatures in the combustion chamber, temperature-dependent material properties can also be incorporated to study their effects on performance of oblique detonation wave engine. Moreover, viscous simulations can be performed to run CHT simulations in wedge/ramp structure and study fluid-thermal-structural interactions of detonation waves formed over a ramp/wedge structure. This is recommended since when high temperatures come into

play, aeroelastic phenomenon gets more pronounced, affecting combustor performance to a higher degree.

CHAPTER SIX: REFERENCES

1) Adhikari, S. (2022). *Study the Characteristics of Oblique Detonation Wave in Blunted Wedge Geometry.* Nanjing: Nanjing University of Aeronautics and Astronautics.

2) Adhikari, S., Hao, T., & Bhattrai, S. (2022). Development and application of a high-speed reacting flow solver in OpenFOAM. *Journal of Innovations in Engineering Education*, 15-24.

3) Anderson, J. (2019). *Hypersonic and High-Temperature Gas Dynamics.* Virginia: AIAA.

4) Bhattarai, S., & Tang, H. (2016). Formation of near-Chapman-Juguet oblique detonation wave over a dual-angle ramp. *Aerospace Science and Technology*.

5) Bhattrai, S. (2021). *Experimental and numerical study of hypersonic aeroelastic intakes.*

6) Bhattrai, S., McQuellin, L. P., Currao, G. M., Neely, A. J., & Buttsworth, D. R. (2021). Experimental Study of Aeroelastic Response and Performance of a Hypersonic Intake Ramp. *Journal of Propulsion and Power*.

7) Bhattrai, S., McQuellin, L. P., Currao, G., Neely, A., & Buttsworth, D. R. (2018). Influence of hypersonic fluid-structure interaction on the control authority of a trailing-edge flap. *22nd AIAA International Space Planes and Hypersonics Systems and Technologies Conference.*

8) Blain, L. (2021, May 12). *World First: Oblique wave detonation engine may unlock Mach 17 aircraft.* Retrieved from NEW ATLAS: https://newatlas.com/aircraft/oblique-wave-detonation-engine-hypersonic-ucf/

9) Bulat, P., & Volkov, K. (2016). Detonation Jet Engine. Part II - Construction Features. *International Journal of Environment & Science Education*.

10) Currao, G., Bhattrai, S., & Neely, A. (2020). Fluid-Thermal-Structure Interactions on a Hypersonic Two-Dimensional Intake. *ISABE 2019.* Canberra, AUS.

11) Deiterding, R., & Mauch, S. (2007). A Virtual Test Facility for Simulating Detonation-and-Shock-Induced Deformation and Fracture of Thin Flexible Shells. *International Journal for Multiscale Computational Engineering*.

12) Dhondt, G., & Wittig, K. (2023, August 1). *A Free Software Three-Dimensional Structural Finite-Element Program*. Retrieved from CALCULIX: http://www.calculix.de

13) Dudebout, R., & Sislian, J. (1998). Numerical Simulation of Hypersonic Shock-Induced Combustion Ramjets. *Journal of Propulsion and Power*, 869-879.

14) Dunlap, R., & Brehm, R. (1958). A Preliminary Study of the Apllication of Steady-State Detonative Combustion to a Reaction Engine . *Jet Propulsion*, 451-456.

15) Geuzaine, C., & Remacle, J.-F. (2009). A three-dimensional finite element mesh generator with built-in pre- and post-processing facilities. *International Journal for Numerical Methods in Enginering* , 1309-1331. Retrieved from Gmsh.

16) Haghgoo, M., & Babaei, H. (2022). Dynamic response of thin triangular plates under gaseous detonation loading . *materialstoday communication*.

17) Hayashi, K. (2021). *Design of Detonation Chamber for Destructing Chemical Warfare Materials.* CWD Project Center.

18) Hertzberg, A., & Bruckner, A. (2012). Ram accelerator - A new chemical method for accelerating projectiles to ultrahigh velocities. *AIAA Journal*, 195.

19) Hu, C., & Zhang, X. (2018). A fluid-structure coupling method to obtain parameter distributions in a combustion chamber with moving boundaries. *Applied Thermal Engineering*, 1048-1054.

20) Kee, R. J., Rupley, F. M., & Miller, J. A. (1989). *CHEMKIN-II: A FORTRAN Chemical Kinetics Package for the Analysis of Gas-Phase Chemical Kinetics.*

21) Khatir, Z., & Pozarlik, A. (2007). Numerical Investigations of Fluid Structure Interaction Between Unsteady Flow and Vibrating Linear in a Combustion

Chamber. *International Conference on Computational Methods for Coupled Problems in Science and Engineering* . Barcelona: CIMNE.

22) Lee, J. H. (2008). *The Detonation Phenomenon.* Cambridge University Press.

23) Malekan, M., & Khosravi, A. (2019). Deformation and fracture of cylindrical tubes under detonation loading: A review of numerical and experimental analysis. *International Journal of Pressure Vessels and Piping* .

24) National Institute of Standards and Technology, U. D. (2013). *NIST-JANAF Thermochemical Tables*. Retrieved from National Institute of Standards and Technology: https://janaf.nist.gov/

25) OpenCFD Ltd. (2023, December). *ESI OpenFD Release OpenFOAM v2112*. Retrieved from OpenFOAM: https://www.openfoam.com/news/main-news/openfoam-v2112

26) Powers, J. M. (1994). Oblique Detonations: Theory and Propulsion Applications. In J. Buckmaster, & T. Jackson, *Combustion in High-Speed Flows* (pp. 345-371). Springer, Dordrecht.

27) preCICE. (2023, December). *The coupling library for partitioned multi-physics simulations*. Retrieved from preCICE: http://www.precice.org

28) Rosato, D., Thornton, M., Sosa, J., Bachman, C., Goodwin, G., & Ahmed, K. (2021). Stabilized detonation for hypersonic propulsion. *PNAS*.

29) Sourav, S., Karnick, T., Singh, M., & Kartik. (2023). Flutter Instability in Supersonic Flow over a Flexible Compressible Ramp. *57th 3AF International Conference on Applied Aerodynamics.* Bordeaux, France.

30) Verreault, J., Higgins, A. J., & Stowe, R. A. (2012). Formation and Structure of Steady Oblique and Conical Detonation Waves. *AIAA Journal*.

31) Xia, Y., & Sharkey, P. (2022). Prediction of Thermoacoustic Instability and Fluid-Structure Interactions for Gas Turbine Combustor. *Journal of Engineering and Gas Turbines Power*.

32) Zhang, Z., Wen, C., Yuan, C., Liu, Y., Wang, C., & Jiang, Z. (2022). An experimental study of formation of stabilized oblique detonation waves in a combustor. *Combustion and Flame* .

APPENDIX

Python Code for performing FFT on ramp-tip deflection data

```python
# Importing necessary modules
import numpy as np
import matplotlib.pyplot as plt


# Open the log file, remove the first line and split every line based on the delimiter
log = open('precice-Solid-watchpoint-Flap-Tip.log2', 'r').read().splitlines()
log = log[1:] # Removing the first line containing column-title
log = [line.split(' ') for line in log]


# Initialize empty array for time and displacement
t = []
y_displacement = []


# Accessing t and y values from log files. Then, store on their individual array
for line in log:
        t.append(line[0])
        y_displacement.append(line[4])


t = np.array(t)
y_displacement = np.array(y_displacement)


# FFT
def fft_func(time, y):
        dt = 1e-5#time[1] - time[0]
        n = len(y)
        fhat = np.fft.fft(y,n)
        PSD = fhat*np.conj(fhat)/n
        freq = ( 1 / (dt*n)) * np.arange(n)
        L = np.arange(1, np.floor(n/2), dtype = 'int')
```

```python
        return [PSD[L], freq[L]]


psd, freq = fft_func(t,y_displacement)


#finding the index of max amplitude and passing that index to frequency array
print('frequency at which max amplitude occurs = ', freq[np.array(psd).argmax()])
print(' max amplitude  = ', psd.max())


plt.plot(freq,psd)
plt.xlabel('frequency')
plt.ylabel('amplitude')
plt.xlim(0,2000)
plt.yscale('log')
plt.show()
```

Python code to calculate induction length and extract its modes of movement via FFT

```python
import numpy as np
import matplotlib.pyplot as plt
import os


startTime = 1*10**-5
timeArray = []
xArray    = []
yArray    = []
lengthAlongRamp = []


INDEX = 0
directory = '/path/to/dataFolder'
files = sorted(os.listdir(directory))
for filename in files:
        if filename.endswith('.csv'):
                with open(os.path.join(directory, filename)) as f:
                        log = f.read().splitlines()
                        log = log[1:]
                        log = [line.split(',') for line in log]

                        h2o = []
                        x = []
                        y = []

                        for line in log:
                                h2o.append(float(line[5]))
                                x.append(float(line[12]))
                                y.append(float(line[13]))
```

```python
                    h2o = np.array(h2o)
                    x = np.array(x)
                    y = np.array(y)


                    maxh2o = max(h2o)


                    h2oFiltered = h2o[h2o<=0.01*maxh2o]
                    xFiltered = x[h2o<=0.01*maxh2o]
                    yFiltered = y[h2o<=0.01*maxh2o]


                    h2o = h2oFiltered


                    index = np.size(h2o) # finding index of required 1% H2O
concentration
                    #print('The required x-coordinate =', x[index-1]*10**3, ' mm')


                    xAdd = x[index-1]*10**3 # in mm
                    yAdd = y[index-1]*10**3
                    lAdd = np.sqrt(xAdd**2+yAdd**2)


                    timeArray.append((INDEX+1)*1*10**-5)
                    xArray.append(xAdd)
                    yArray.append(yAdd)
                    lengthAlongRamp.append(lAdd)
                    maxh2oArray.append(maxh2o)
                    INDEX += 1


print('timeArray = ', timeArray)
print('xArray = ', xArray)
print('yArray = ', yArray)
print('lengthAlongRamp = ', lengthAlongRamp)
```

```python
lengthAlongRamp = np.array(lengthAlongRamp)
timeArray = np.array(timeArray)


# Plotting maximum value of H2O versus time
plt.plot(timeArray, maxh2oArray)
plt.show()


#Performing FFT on timeArray and lengthAlongRampArray
def fft_func(time, y):
        dt = 1e-5#time[1] - time[0]
        n = len(y)
        fhat = np.fft.fft(y,n)
        PSD = fhat*np.conj(fhat)/n
        freq = ( 1 / (dt*n)) * np.arange(n)
        L = np.arange(1, np.floor(n/2), dtype = 'int')
        return [PSD[L], freq[L]]


psd, freq = fft_func(timeArray,lengthAlongRamp*10**-3)


#finding the index of max amplitude and passing that index to frequency array
print('frequency at which max amplitude occurs = ', freq[np.array(psd).argmax()])
print(' max amplitude  = ', psd.max())


plt.plot(freq,psd)
plt.xlabel('Frequency (Hz)')
plt.ylabel('Distance from ramp tip (mm)')
plt.yscale('log')
plt.show()


#Plotting induction length as a function of time
plt.plot(timeArray, lengthAlongRamp)
plt.xlabel('time (s)')
```

```
plt.ylabel('induction distance wrt ramp tip (mm)')
plt.show()
```
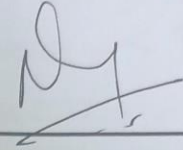
sandipGewaliThesis-plag-check-version-2.pdf

13%
SIMILARITY INDEX

PRIMARY SOURCES

1. vdoc.pub
   Internet
   110 words — 1%

2. unsworks.unsw.edu.au
   Internet
   102 words — 1%

3. eprints.soton.ac.uk
   Internet
   100 words — 1%

4. www.researchgate.net
   Internet
   99 words — 1%

5. tel.archives-ouvertes.fr
   Internet
   95 words — 1%

6. Sudip Bhattrai, Liam P. McQuellin, Gaetano M. D. Currao, Andrew J. Neely, David R. Buttsworth. "Experimental Study of Aeroelastic Response and Performance of Hypersonic Intake Ramp", Journal of Propulsion and Power, 2021
   Crossref
   82 words — 1%

7. www.ncbi.nlm.nih.gov
   Internet
   56 words — 1%

8. Matthew Grismer, Joseph Powers. "Calculations for steady propagation of a generic ram
   51 words — < 1%